CHALMERS
UNIVERSITY OF TECHNOLOGY

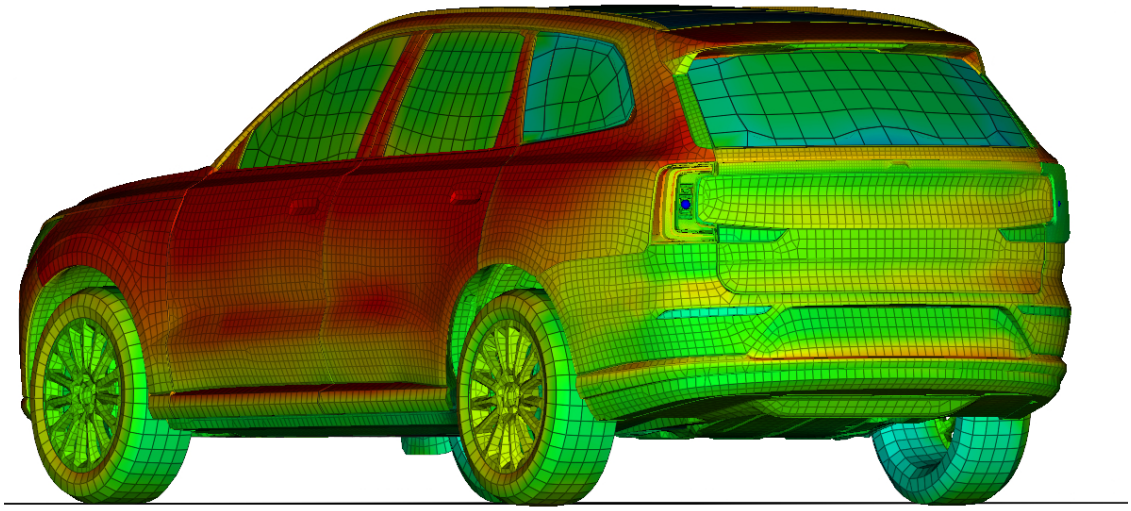

Temperature Prediction in Car Lamps Using Sun Load Data

A simulation model development study for the rear lamps of the Volvo $EX90$

Master Thesis in Applied Mechanics

BILAL MOHAMMED SAJJAD SIDDIQUI

DEPARTMENT OF MECHANICS AND MARITIME SCIENCES

CHALMERS UNIVERSITY OF TECHNOLOGY
Gothenburg, Sweden 2025
www.chalmers.se

Master's thesis 2025

Temperature Prediction In Car Lamps Using Sun Load Data

A simulation model development study for the rear lamps of the Volvo $EX90$

BILAL MOHAMMED SAJJAD SIDDIQUI

CHALMERS
UNIVERSITY OF TECHNOLOGY

Division of Fluid Dynamics, Department of Mechanics and Maritime Sciences
Chalmers University of Technology
Gothenburg, Sweden 2025

Temperature Prediction In Car Lamps Using Sun Load Data
A simulation model development study for the rear lamps of the Volvo $EX90$
BILAL MOHAMMED SAJJAD SIDDIQUI

© BILAL MOHAMMED SAJJAD SIDDIQUI, 2025.

Supervisor: Kevin Ståhl and Britta Mattsson, Volvo Car Corporation
Examiner: Lars Davidson, Division of Fluid Dynamics, Mechanics and Maritime Sciences

Master's Thesis 2025
Division of Fluid Dynamics, Department of Mechanics and Maritime Sciences
Chalmers University of Technology
SE-412 96 Gothenburg
Telephone +46 31 772 1000

Cover: Temperature Prediction In Car Lamps Using Sun Load Data.

Typeset in LaTeX
Printed by Chalmers Reproservice
Gothenburg, Sweden 2025

Temperature Prediction In Car Lamps Using Sun Load Data
A simulation model development study for the rear lamps of the Volvo $EX90$
BILAL MOHAMMED SAJJAD SIDDIQUI
Department of Mechanics and Maritime Sciences
Chalmers University of Technology

Abstract

Heat-sensitive materials and components, such as batteries, sensors, cameras, and polymeric materials, are a significant part of most cars on the market. To avoid damage to these parts, it is important to know what temperatures they will be subjected to. Sun Load Data (SLD) uses loads generated by the sun, solar radiation, to predict temperatures in different areas of the car.

This thesis aims to conduct an SLD study using a detailed rear lamp model of the Volvo $EX90$, which also includes the different material properties for each component, such as emissivity, transmittance, reflectivity and absorptivity. The material properties of the different components that make up the lamp will be measured and used as part of the input parameters. Different types of convection (using the lump capacitance model $0-D$ or $3-D$) are simulated and compared, taking into account the level of accuracy and runtime. Different days are also selected to be used as the input weather file, making an attempt at extending the correlation to days when the ambient or part temperature is the highest. The effect of the external wind as well as the LED light source on the temperature readings are also taken into account.

The developed virtual model can be used in the early development phase for requirement setting, material choice, and the geometric design of the lamp. It can be used as an early checkpoint to decide whether the aforementioned parameters are ideal. This will therefore eliminate the situation where the vehicle is already in the physical testing phase, and the lamp experiences performance or aesthetic failure. Areas with potential for improvement are discussed together with their probable reasons, along with actions to mitigate them.

Keywords: SLD, emissivity, transmittance, solar irradiation, absorptance, conduction, convection.

Acknowledgements

I would like to extend my sincere thanks to Kevin Ståhl, who in his role as the supervisor provided adept support and guidance needed throughout the thesis. Prof. Lars Davidson as the examiner for this thesis, provided invaluable feedback, insights and additional guidance with an emphasis on learning and making an impact with the work done through this project.

A special thanks goes to Britta Mattsson, Per Tobiasson, Johan Granath, Jonas Horkeby, and HansPetter Aasen from the Material Center at *VCC* for their valuable input through their vast experience in working with this topic. Björn Ratama and Renaud Gutkin, for their insights, continued interest and encouragement throughout the project duration. The *CAE* team at *VCC* Safety Center, for being helpful and providing a friendly work environment. Steve Patterson and Kameswara Kethireddy from *ThermoAnalytics*, who provided crucial software and technical understanding required to build and ensure that the model is accurate as possible.

A big thank you to Volvo Car Corporation, for providing me with the workspace, necessary resources, and most importantly the opportunity to carry out this research.

Lastly, I would like to thank my parents, family and friends for being pillars of continuous support and encouragement.

Bilal Mohammed Sajjad Siddiqui, Göteborg, August 2025

List of Acronyms

Below is the list of acronyms that have been used throughout this thesis listed in alphabetical order:

CFL	Courant-Friedrichs-Lewy
HID	High Intensity Discharge
LED	Light Emitting Diode
RF	*RapidFlow*
SLD	Sun Load Data
VCC	Volvo Car Corporation

Nomenclature

Below is the nomenclature of indices, sets, parameters, and variables that have been used throughout this thesis.

Indices

i , $i-1$	Iteration indices

Parameters

$\mathcal{A}$	Absorptance
$\mathcal{C}$	CFL Number
n	Iterations
ρ	Reflectance
α	Relaxation Factor
τ	Transmittance
E	Emissivity

Variables

Q	Rate at which a surface receives heat
$Q_{\mathcal{A}}$	Fraction of absorbed heat
Q_{τ}	Fraction of transmitted heat
Q_{ρ}	Fraction of reflected heat
T	Relaxed temperature solution for the current iteration
T_{old}	Computed temperature from the previous iteration

T_{new}	Computed temperature solution for the current iteration without relaxation

Contents

List of Figures

List of Tables

1
Introduction

This master thesis is designed to last for approximately 20 weeks, with supervisors from both, the durability department as well as the materials center, as the results obtained from this project will require inputs from and also provide important data to both teams.

1.1 Organization

Volvo Car Corporation, known widely for their safety standards, houses one of the world's most advanced crash test facilities along with state-of-the-art testing capabilities. The safety center plays a crucial role in not only ensuring that Volvo continues to pioneer automotive safety, but also customer experience. This thesis falls under the durability subteam where trim and closure analyses are performed.

Table 1.1: Safety center organization

Hierarchy	Team
Domain	`Vehicle Engineering`
Subdivision	`Safety Center`
Specialization	`Durability Trim and Closure Analysis`

1.2 Background

An automobile is an assembly of numerous complex components that allow it to perform at an accepted level while also providing aesthetic and experiential pleasure to the user. These components are tested rigorously in order to identify and rectify any issues that may arise during its function cycles. Not only can it help in reducing the overall weight of the vehicle and thereby improving fuel efficiency [1], it is far easier and affordable to iterate through different material choices in a virtual model, than when the vehicle is already in production. An area of focus is the temperature that a given component experiences. Heat sensitive materials are especially singled-out, and tested through wide and long cycles to ensure durability and reliability. Their failure could be detrimental to the performance of the vehicle, thereby affecting customer experience.

Heat load is a common scenario where prolonged exposure to the sun results in either aesthetic (deformations, delaminations, etc.) or functional failures. A solution may be

to either change the material being used or improve the design to be able to withstand such thermal loads. In order to avoid failure, the maximum temperature that the parts are subjected to needs to be identified. Predictive temperature models are seen as a way to virtually test the performance of components before actual physical tests are performed. This can accelerate the development process by reducing the time, effort, and cost that would otherwise be required in a physical setup. However, it is important to remember that computational methods are not devoid of limitations. Industry-scale simulations can take very long to produce results, which makes the involvement of assumptions in the solver setup key.

1.3 Aim

The focus will be on developing a thermal model for predicting temperatures in car lamps. This is an area of the car that can easily reach high temperatures that could potentially cause overheating or damage to structural materials. The lamps in a car are complex with many different parameters that can affect the temperature, for example, radiation through transparent materials, heat conductivity, convection, wind, and heat generating components. To obtain an accurate prediction, the model should handle the most important factors when it comes to temperature prediction. The main outcome of this thesis would be to determine and construct a correlated thermal model of the rear lamp, together with recommendations of which factors are important to consider when performing the analysis.

Figure 1.1: Rear lamp of the Volvo $EX90$

1.4 Literature

The lamps of an automobile have been an area of interest for some time now mainly because of their impact in case of damage. Overheating of the lamp compartment can lead to degradation and discoloration of materials, causing failure. Higher temperatures can also reduce the efficiency of the lamp, along with other issues such as lens warping. The use of light emitting diode (LED) and high intensity discharge

(HID) bulbs in modern automobiles require shorter focal points, which in turn leads to unwanted focus on plastic aesthetic parts used around the lenses. Additionally, due to parallelism of the sun rays [5], the focal point is more intense compared to other light sources. In addition to thermal simulation, studies have also included calculation of the critical angle and inclination angle, along with ray tracing analysis which is finally compared to the test setup data to identify hot-spots and therefore carry out the necessary design changes [4].

Among the various parameters that influence the heat resistance between different parts is natural convection. However, this is tricky as the lamp is an assembly of complex geometries as mentioned before. Some intricate parts are in the order of millimeter in magnitude. In such cases, the mesh density is of importance if accurate information is to be captured. This results in a mesh with millions of nodes generated, significantly increasing the computational time. Interesting methods such as the Surface Heat Transfer (SHT) method have been developed and used to evaluate the natural convection inside the lamps with reasonable precision [10]. Some other practical environmental applications were also studied where the effect of moisture was also considered. This was done by calculating the absorption and desorption of moisture between the inner parts of the lamp and the fluid within the assembly, by assuming there exists an analogy between heat transfer and moisture transfer [9].

1.5 Delimitations

It is clear that the scope of this study can be vastly extended to many different scales which also means greatly increasing the amount of information needed to solve such scenarios.

1. **Components:** In this thesis, the main focus would be only on the rear lamps of the car. This means that other heat sensitive components (though they are important as well) are not discussed in this report.

2. **Coupling:** Coupled heat transfer analysis using other softwares such as $ABAQUS$ will not be performed. However, heat transfer due to convection, conduction, radiation, etc. are considered and made a part of the solver setup in $TAITherm$.

3. **Vehicle Scenario:** The vehicle will be studied and simulated on only the parked condition. This is because a driving car brings in a different dimension to the nature of analysis, particularly because the parts would cool differently, and the fact that the lights are turned on or off multiple times (for example, when driving in traffic) which will result in a fluctuation of temperature of the lamp.

2
Theory

When two systems are brought in contact with one another, either directly or indirectly through a wall, they communicate in the form of energy transfer, either in the form of work or heat. The three fundamental modes of heat transfer are conduction, convection, and radiation. The amount of heat transferred, for example, largely depends on the individual states of the two systems, as well as the wall that separates them (if present). They may also not transfer any heat at all if they are connected by a diathermal wall (non-adiabatic) and do not experience any heat transfer for a fixed time period.

2.1 Convection

Convection takes place in the presence of a fluid medium (air in this study). When the medium flows over the car, the difference in their temperatures causes a transfer of heat between them. The transport of heat is linked with the motion of the particles themselves, i.e., if the driving force of the medium is buoyancy caused by the density variation due to the difference in temperature in the fluid, it is referred to as *natural* or *free* convection. Similarly, if the fluid motion is set up artificially, using a fan, for example, it is referred to as *forced* convection [8]. This thesis relates to the free convection type as wind is used as an input in the simulation, which is not caused artificially. The basic relation is described by Newton's heat convection equation,

$$q = \frac{Q}{A} = h(T_s - T_\infty) = h\Delta T \tag{2.1}$$

It is seen that the velocity of the fluid is 0 at the wall (no-slip condition), which means heat is transferred only via conduction. Seeing this dependency on the difference in temperature, it is worthwhile to understand the different boundary layers [6] and where they occur. The boundary layer is broadly divided into two main regions: a "near-wall" region where the temperature and velocity gradients are large, and a region outside this boundary where the gradients are not so high anymore. The thickness of this boundary is roughly defined as the distance from the surface where the local field value is 99% of the free-stream function (velocity or temperature).

2.2 The Velocity Boundary Layer

If a flow over a flat plate is considered, the flow upstream (before it encounters the plate) is uniform. After coming in contact with the plate, in order to satisfy

the no-slip condition, the fluid particles in contact with the plate surface have 0 velocity. As we observe the particles farther away from the surface (normal to the plate), there is a reduction in the velocity gradient until the boundary layer thickness is reached, beyond which the gradient is approximately the same as its free stream value. This retardation in motion close to the wall is due to the shear stress forces that exist in the fluid. The thickness of this boundary layer is defined as the point at which the velocity of the particles has reached 99% of the free stream velocity.

Another difference is the *nature* of the fluid flow. A flow regime can be distinguished based on whether it is laminar or turbulent. Both regimes also have different boundary layers. Depending on the type of fluid and surface, at some critical distance, x_c, the laminar regime will start to transition and eventually become turbulent. In the turbulent region, the velocity profile in the boundary is a lot more uniform. This could be due to the presence of irregular mixing of the fluid flow, which also results in a thicker boundary layer.

2.3 Recirculation Zone

A recirculation zone is a region of fluid flow where the flow reverses due to an adverse pressure gradient or a sharp change in geometry. This low-pressure region draws the velocity from the free-stream to create a *backflow*, where the fluid moves in the direction opposite to that of the free-stream. These vortex-like structures are also characterised by their low velocities.

2.4 Thermal Radiation

All bodies whose temperature is above the point of absolute zero ($0\ K$) emit energy in the form of radiation. The magnitude of the energy is directly proportional to the temperature to which the body is subjected. Unlike conduction or convection, radiation does not require any medium between the two communication bodies to exchange energy. In other words, heat transfer by radiation takes place perfectly in a vacuum. To be able to distinguish one form of radiation from another, we look at the electromagnetic spectrum, where the wavelengths are the main source of segregation.

Across the entire spectrum, we are only able to see a small portion, called the visible spectrum. In addition to this, our senses can also detect a slightly wider range which also includes infrared light. These ranges are together known as the the spectrum of the *Thermal Radiation*. They are able to heat up bodies which in-turn leads them to emit energy to be absorbed by other bodies. As already mentioned, a small portion is also visible, a common example being the colour of a metal becoming more red as it is heated up.

2.4.1 Absorption, Transmission and Reflection

All incident rays on the surface of a body are either absorbed, transmitted or reflected. Let Q be the rate at which the surface receives heat (incident), then the absorption ($\mathcal{A}$), transmission (τ) and reflection (ρ) fractions are as follows,

$$Q = \begin{cases} \mathcal{A}, & \frac{Q_{\mathcal{A}}}{Q} \\ \tau, & \frac{Q_{\tau}}{Q} \\ \rho, & \frac{Q_{\rho}}{Q} \end{cases} \tag{2.2}$$

where, $Q_{\mathcal{A}}$, Q_{τ} and Q_{ρ} is the amount of heat absorbed, transmitted and reflected, respectively. We can already see that in order to satisfy the principle of conservation of of energy,

$$\mathcal{A} + \tau + \rho = 1 \tag{2.3}$$

Equation 2.3 is valid only on surfaces of finite thickness, and the values lie between 0 and 1. Some additional understanding is tabulated in 2.1 with the illustration in figure 2.1,

Table 2.1: Surface properties

$\mathcal{A} = 0$	Non-absorbing surface or a white surface
$\mathcal{A} = 1$	Perfect absorber or a black surface
$\tau = 0$	Opaque surface
$\tau = 1$	Perfectly transparent surface
$\rho = 0$	Non-reflecting surface
$\rho = 1$	Perfect reflector

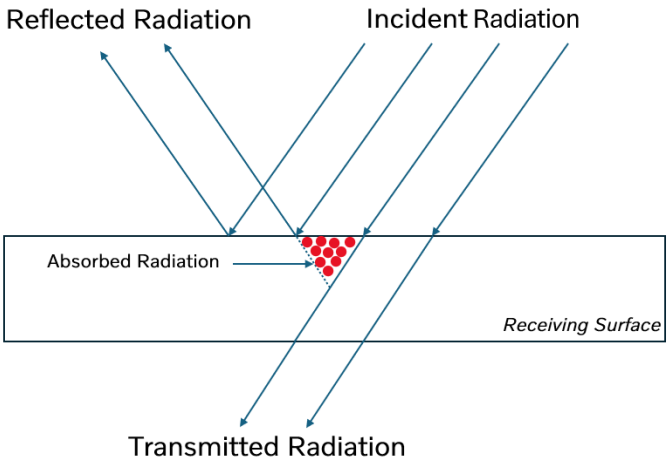

Figure 2.1: Visual representation of absorptance, reflectance and transmittance

2.4.2 Spectral and Diffuse Reflection

For a standard body, we know that every incident ray has a reflected ray. The angle that the reflected ray makes with the normal is what differentiates spectral and diffuse reflection. If the incident radiation falling on a smooth surface such as a mirror or a polished surface makes the same angle with the normal as the reflected radiation, then it is said to be a case of *specular* reflection. On the other hand, if after incidence, the reflected radiation is spread across in different directions, it is known as $diffuse$ reflection. This is seen for rough surfaces. Most bodies are often approximated to have one of the above two types of reflection based on their surface. In this study, all surfaces are defined to have diffuse reflection.

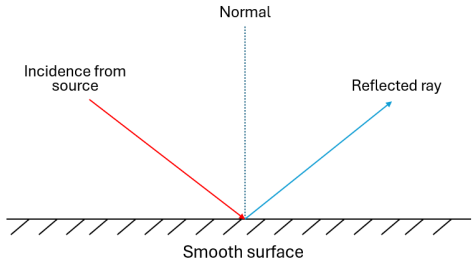

($a.$) Specular Reflection

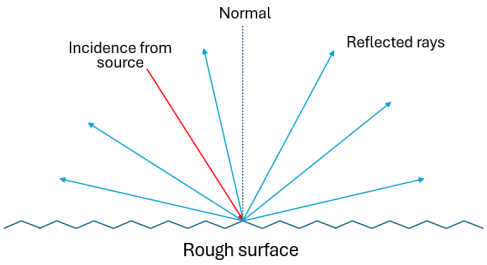

($b.$) Diffuse Reflection

Figure 2.2: Types of reflection

2.5 Kirchhoff's Law

When a body is placed in an enclosure with a temperature T, the two systems exchange energy until they reach thermal equilibrium. Once achieved, the ratio of the total emissive power to its absorptivity will be the same for all bodies,

$$\frac{E}{\mathcal{A}} = f(t) \tag{2.4}$$

where the $R.H.S$ indicates that this ratio is a function of temperature. Now, we know that the emissive power will be the greatest for a body when $\mathcal{A} = 1$, and,

$$E = E_b \tag{2.5}$$

where E_b is the emissivity of a black body. By the definition of total emissivity,

$$\varepsilon = \frac{E}{E_b} \tag{2.6}$$

Substituting equations 2.6 and 2.5 into 2.4, we get,

$$\mathcal{A} = \varepsilon \tag{2.7}$$

This relation is known as *Kirchoff's Law* and is subject to the restrictions of the presence of thermal equilibrium and an isothermal enclosure.

3
Methods

All the processes involved in this thesis are broadly divided into pre-processing, solver setup for simulations, and finally, post-processing. Each of these phases requires the use of different tools which will be explained in further detail in the following sections.

3.1 Component Measurement

Some material properties, namely emissivity, absorptivity, transmitivity, etc. are very important to set up the solver with the right data. One of the sample rear lamps was sent to *RISE* to measure and construct the transmittance curve for the lamp lens. In addition to this, the rear lamp available at hand was disassembled into its many components to try and identify what parts can be measured and to what extent. Segregation and documentation of such parts was important as many of them had curved/small surfaces which made it difficult to measure using the measuring guns available at Volvo, shown in *Figures* 3.1 and 3.2.

Figure 3.1: Solar 410 Reflectometer

The measuring device seen in *Figure* 3.1 is the 410−Solar handheld reflectometer. It

measures the reflectance at near-normal incidence for seven spectral bands. It also specifies both spectral and diffuse reflectance.

Figure 3.2: ET 100 Emissometer

The emissometer *ET*100 seen in *Figure* 3.2 calculates the directional and hemispherical emissivity based on reflectance across a range of wavelengths. The fundamental components of *ET*100 are an internal source, a spherical head, and detectors. Once the measurement gun is placed flat on the material to be measured, the light source falls on the surface, and the reflected light in all directions is captured by the sphere (see *Figure* 3.3).

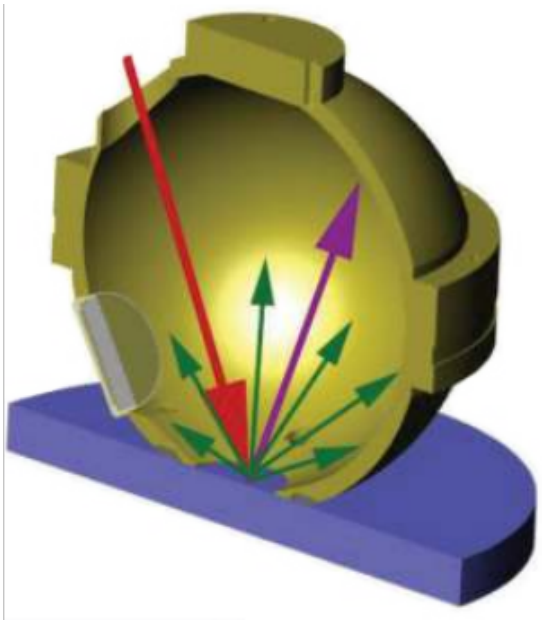

Figure 3.3: Cross section of the spherical head on the target sample surface

Table 3.1 lists the differences between the two measuring devices [11],

Table 3.1: Model comparison

Model	**Solar 410 Reflectometer**	**ET100 Emissometer**
Spectral bands	$335 - 2500$ nm	$1.5 - 21.0$ μm
Calculated properties	Total, diffuse and specular reflectance and absorptance	Directional and hemispherical thermal emissivity
Angle of incidence	20°	20° and 60°

Given how the measurements are carried, there was a concern with regards to measuring transparent parts. This is because it was highly likely that the *red* incident beam from *Figure* 3.3 would pass through the transparent part, and reflect off the surface behind it. This means that the values that are measured would actually be of the surface *behind* the actual part, which would be incorrect. To overcome this, the following steps were taken,

1. Measure and record the emissivity and solar absorptance values from both tools for a completely black surface. A plain black sheet of paper was used in this instance.
2. Place this black surface behind the transparent part, and carry out the measurements as normal.
3. Subtract the measurements of the transparent parts with the black surface behind it, from the measurements of the black paper.
4. This would at least give us approximate values for the transparent parts.

If a solar spectrum curve is not specified, $TAITherm$ uses a constant curve to compute the spectral irradiance. However, in this study, we make use of the $ASTM\ G173-03$ *Standard Solar Spectrum* curve already available in the software, see *Figure* 3.4. This curve is then used to take the weighted average of the transparency curve used in the model.

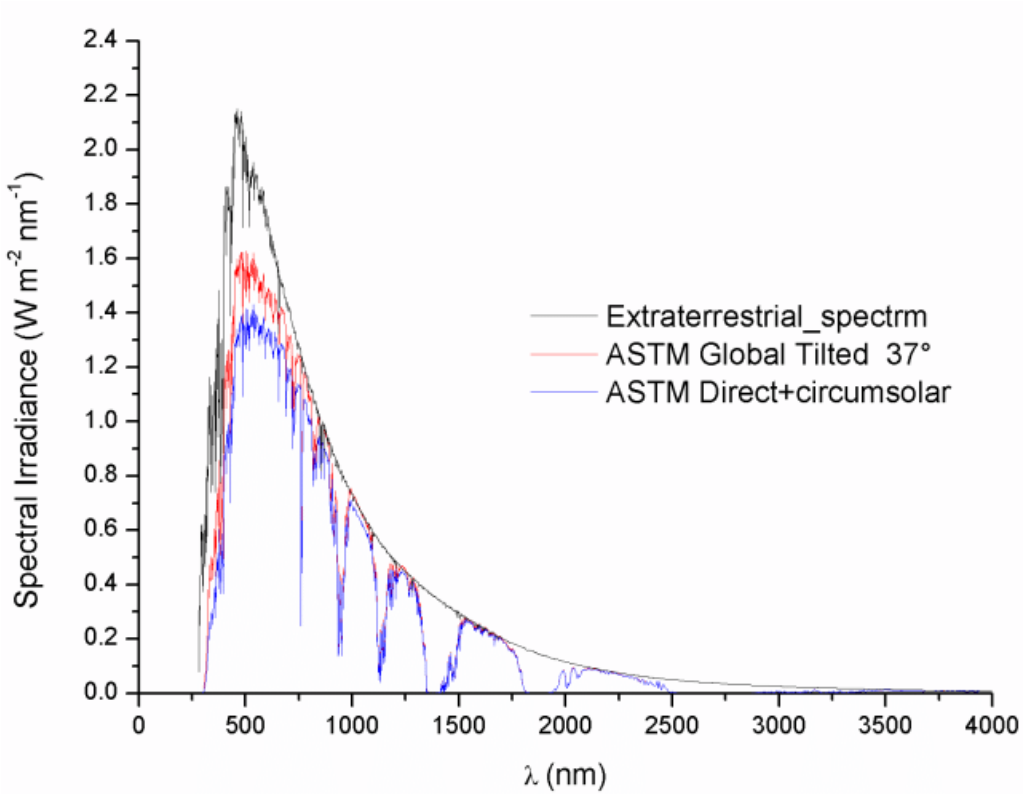

Figure 3.4: *ASTM G*173 − 03 Reference Spectra [3]

3.2 Model Construction

The rear lamp model seen in *Figure* 3.5 shows how the temperature probes are attached at different locations on the face of the lamp.

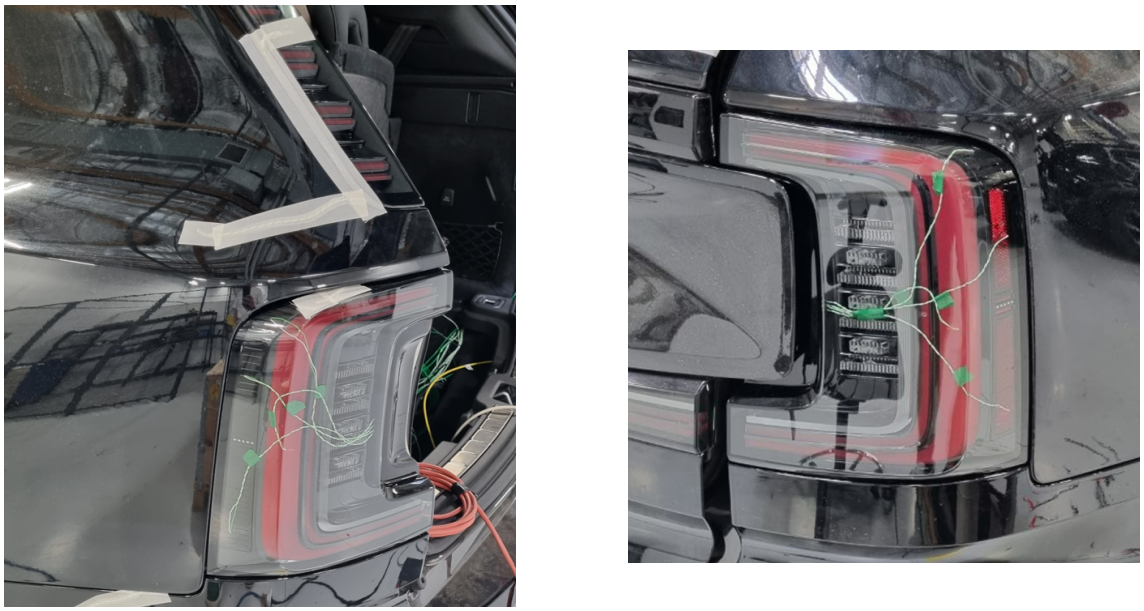

Figure 3.5: Left and right rear lamps, respectively, with temperature probes

It is important to generate a good mesh that is a close representation of its geometric model. Most parts are shell meshed, and ideally are a little coarse in order to reduce the computational time. As mentioned earlier, the material data (obtained from 3.1) of the components are specified here.

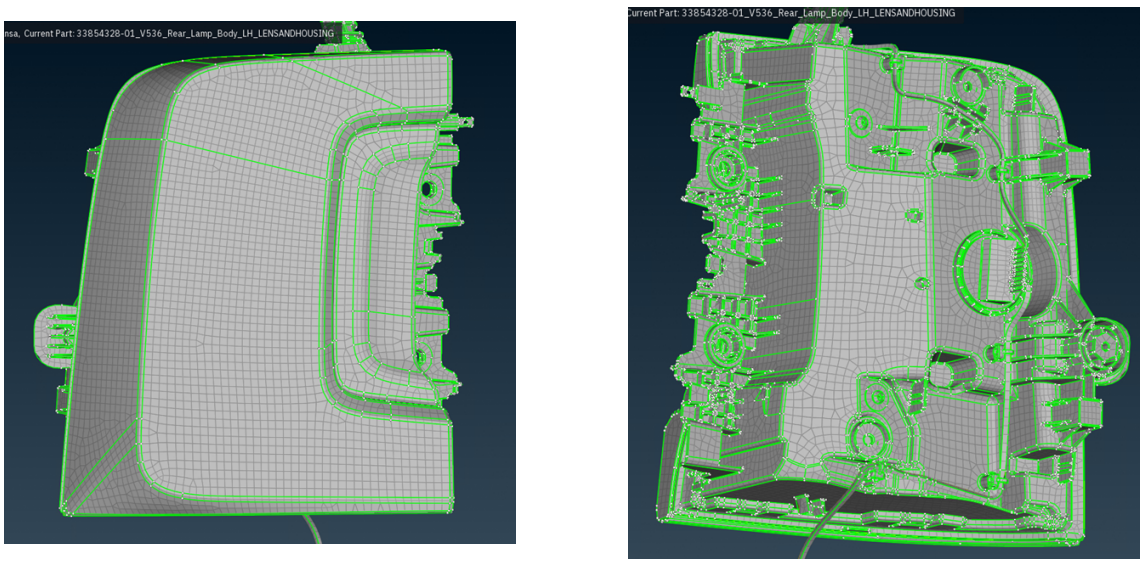

Figure 3.6: Shell mesh representation on the front and back panel, respectively

The front panel of the lamp that receives direct sunlight was mostly flat faced, as can be seen in *Figure* 3.6. Therefore, it is easier to setup a mesh in this region. However, this was not the case for the back panel as shown. This region is dotted with complex geometries. Retaining such intricate geometries in the model led to an

increase in meshing complexity and also increased number of elements significantly. This raised a need to have a simpler model with lesser elements.

3.2.1 Simplification

All cables, connectors, plugs, wire holders, etc. were removed as they were either too small or their contribution to the lamp temperatures would be negligible. *Figures* 3.7 and 3.9 show these changes.

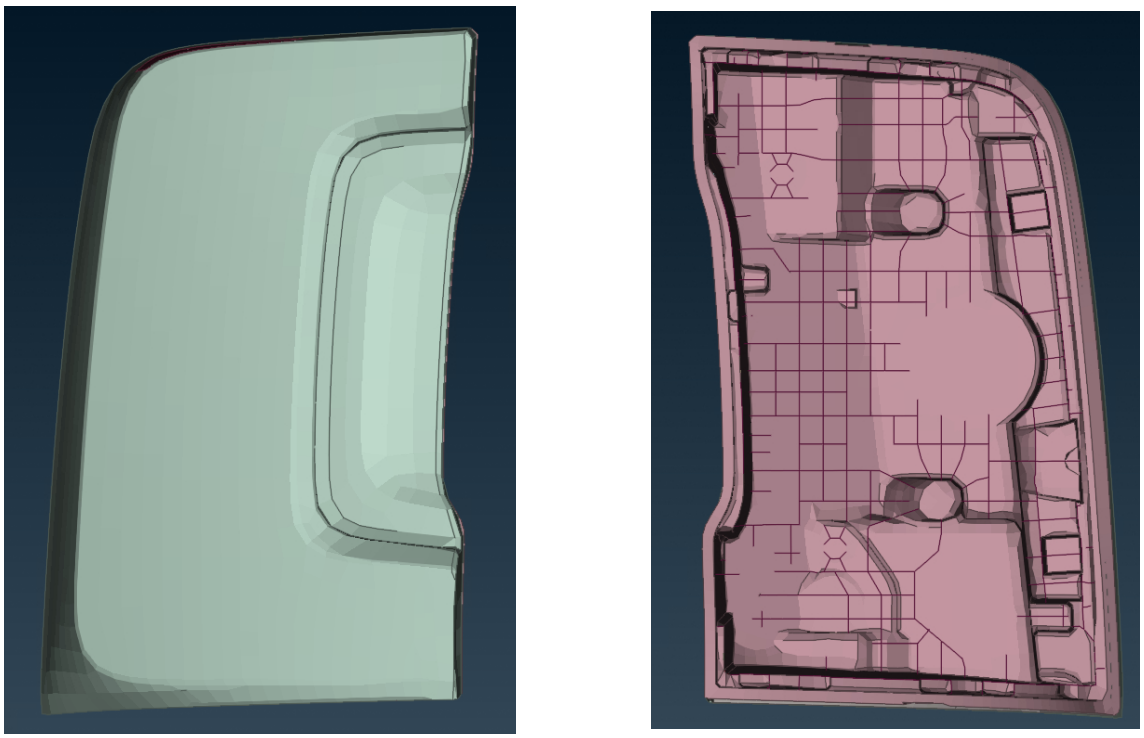

Figure 3.7: Front and rear view of the simplified rear lamp

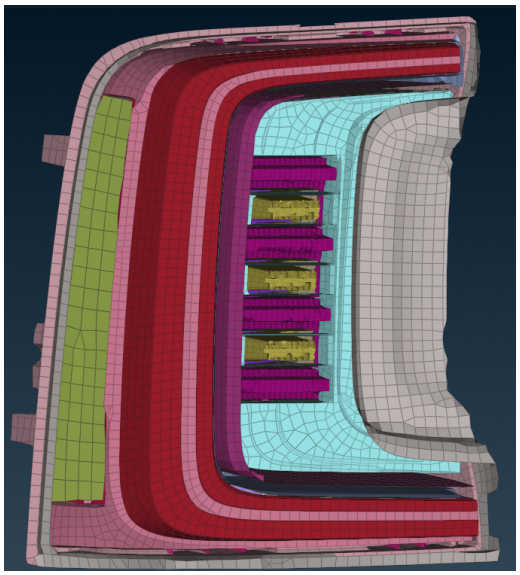

(*a.*) Simplified mesh without the outer lens

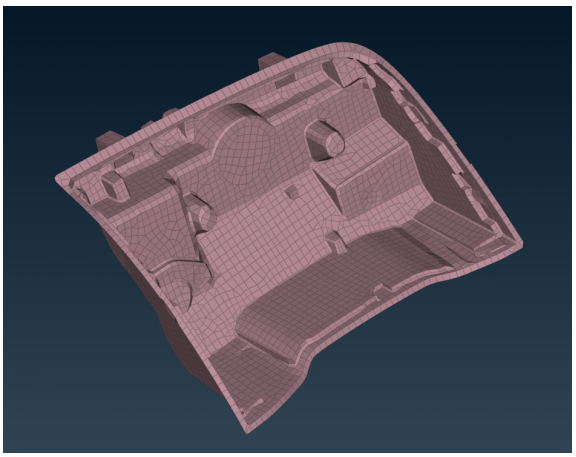

(*b.*) Interior of the simplified mesh

Figure 3.8: (*a.*) Interior view of the simplified mesh

Table 3.2 shows the difference between the two mesh types in terms of the number of elements. The significant reduction in the simplified mesh type helped reduce the run-time by a little more than 2 hours.

Table 3.2: Mesh Type comparison

Mesh Type	**No. of Elements**	**No. of Shells**	**Runtime**
Initial Mesh	254, 254	97.681	6 hrs 28 mins
Simplified Mesh	31, 129	31, 129	4 hrs 23 mins

3.2.2 White Tape Modeling

The small red area on the outer lens in *Figure* 3.9 is the white tape. The white tape is modeled simply by changing the surface properties of some of the elements on the outer lens. These properties are measured values for a standard 3*M Electrical Solar Tape*.

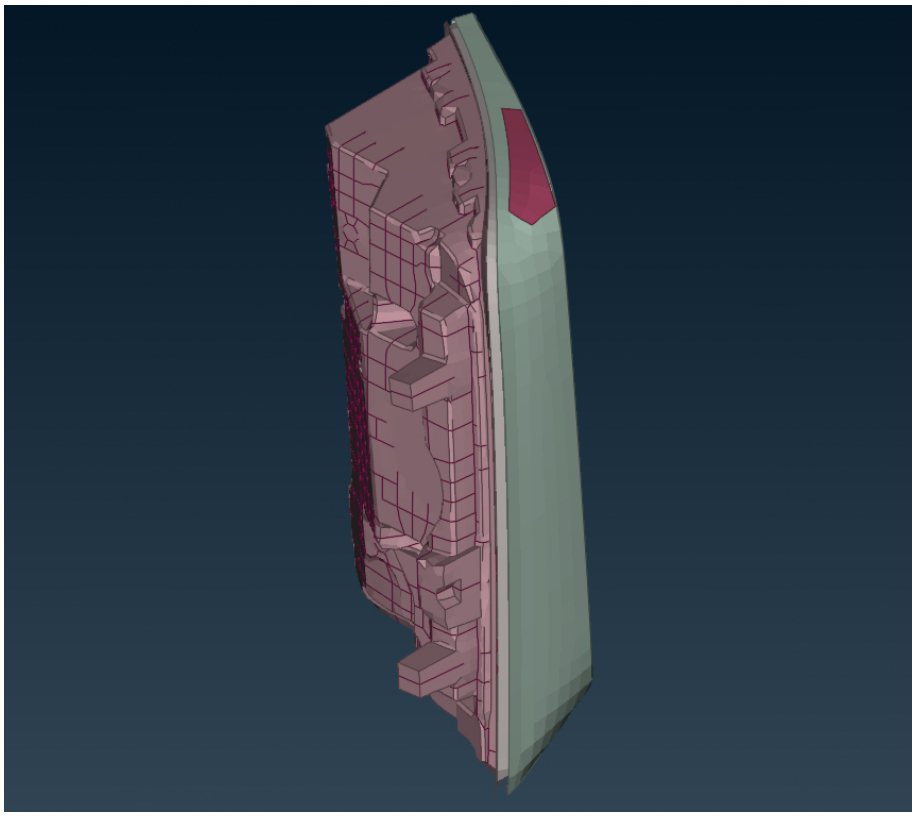

Figure 3.9: Isometric view

These properties are measured values for a standard 3*M Electrical Solar Tape*, see *Figure* 3.10.

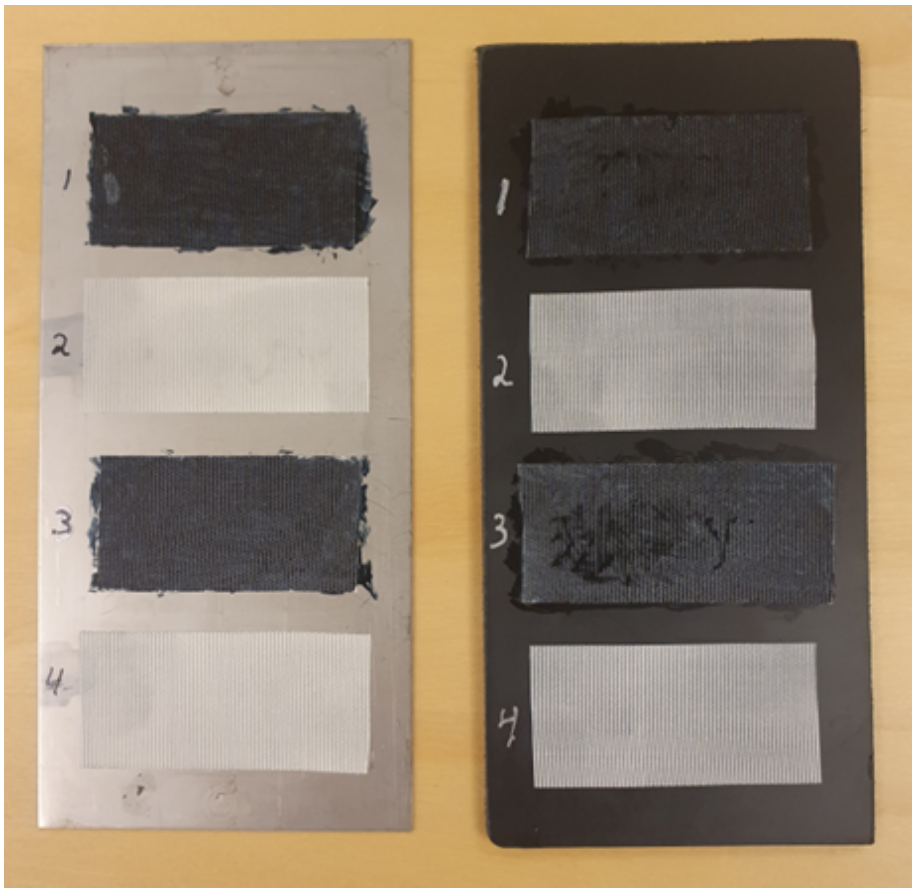

Figure 3.10: Tape surface property measurement setups

Once the model is constructed, it is put into the full-car model, as the surrounding surfaces would have an effect on the lamp temperatures through surface-to-surface radiation, along with a smaller conduction contribution.

3.2.3 Convection

The convection was defined on both surfaces (front and back) of each individual component. The surfaces that were facing outwards, exposed to the outside air, have convection by wind applied. Apart from this, the temperature of the interior parts and surfaces are either estimated using a $0-D$ lumped-capacitance model or a $3-D$ fluid dynamics simulation associated with the domain of the fluid part (which can be either internal or external). The area behind the lamp, which would be in the rear cavity of the vehicle, was assumed to have a negligible effect on the lamp temperature and hence the convection in the volume was computed using the $0-D$ model.

3.3 *TAITherm*

TAITherm is a $3D$ thermal simulation software that covers the complete range of heat transfer phenomena. It solves for thermal radiation, convection, conduction,

and also changes due to environmental conditions.

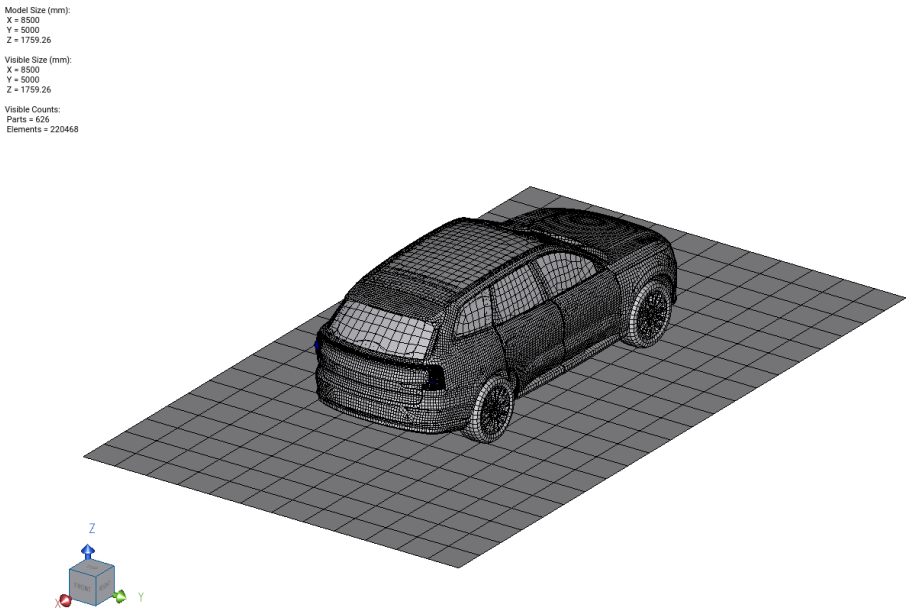

Figure 3.11: *TAITherm* interface

From the experimental setup in Arizona, a weather data file is generated that is used as input in the *TAITherm* model as seen in *Figure* 3.11. The model is run for the same parking direction as the physical setup. Generally, a simulation time range of 12 hours (0800 to 2000) is considered sufficient in most cases to capture the maximum temperatures that occur during a day. The starting time, however, was chosen to be 0300 in order to counter some issues (see Section 5.1) when starting at 0800.

04a

TIME	AIRT	SOLAR	WIND	HUMID	CLOUD	LWIR	WINDIR
0300	27.35	0	2.095	20.4	0	0	310
0305	27.12	0	2.505	20.7	0	0	323
0310	26.95	0	2.02	20.3	0	0	326
0315	27.25	0	1.23	20	0	0	278
0320	27.19	0	0.775	19.8	0	0	301
0325	27.21	0	0.935	20.4	0	0	250
0330	27.19	0	1.06	25.5	0	0	221
0335	27.03	0	0.7	25.8	0	0	248
0340	26.55	0	0.26	25.4	0	0	224
0345	26.13	0	0.595	24.6	0	0	201
0350	26.04	0	0.14	21.2	0	0	272
0355	25.92	0	0.425	23	0	0	294
0400	25.82	0	0.44	24.2	0	0	253
0405	25.72	0	0.65	26.7	0	0	310
0410	25.72	0	0.66	24.9	0	0	326
0415	25.58	0	0.145	26.3	0	0	251
0420	25.56	0.227	1.075	28.8	0	0	265
0425	25.5	0	0.695	27.5	0	0	252
0430	25.46	0	0.44	28	0	0	230
0435	25.51	0	0.83	27.8	0	0	225
0440	25.58	0.227	0.955	25.7	0	0	225
0445	25.63	0	0.975	24	0	0	225
0450	25.49	0	1.065	24	0	0	235
0455	25.05	0	1.025	26.1	0	0	152
0500	24.5	0	0.485	26.7	0	0	188

Figure 3.12: Weather file used as input

3.3.1 Solver Setup

The solution is time-dependent. Since this is not a simple linear solution, an iterative approach is required to accommodate the non-linearity. An initial guess/initial con-

dition is provided and the solver computes the solution at each iteration, seemingly getting better with the number of iterations. We can monitor the temperature value of any given element in the model and see how it varies with the iterations. In the beginning, there will be some oscillations which ideally should iron out eventually as the computation progresses, depicting a converged solution. If these oscillations grow too large, the solution may diverge.

3.3.1.1 Relaxation Factor

Relaxation factors are used to control these oscillations in the solution and therefore prevent divergence. From the example in *Figure* 3.13, let us say that T_{old} is the computed temperature value in the previous iteration n_{i-1}. While according to the solution, the new temperature value should be T_{new}, applying a relaxation factor broadly implies that we instead use 3.1, where T is the *relaxed* solution for the next iteration n_i.

$$T = T_{old} + \frac{1}{2}(T_{new} - T_{old}) \tag{3.1}$$

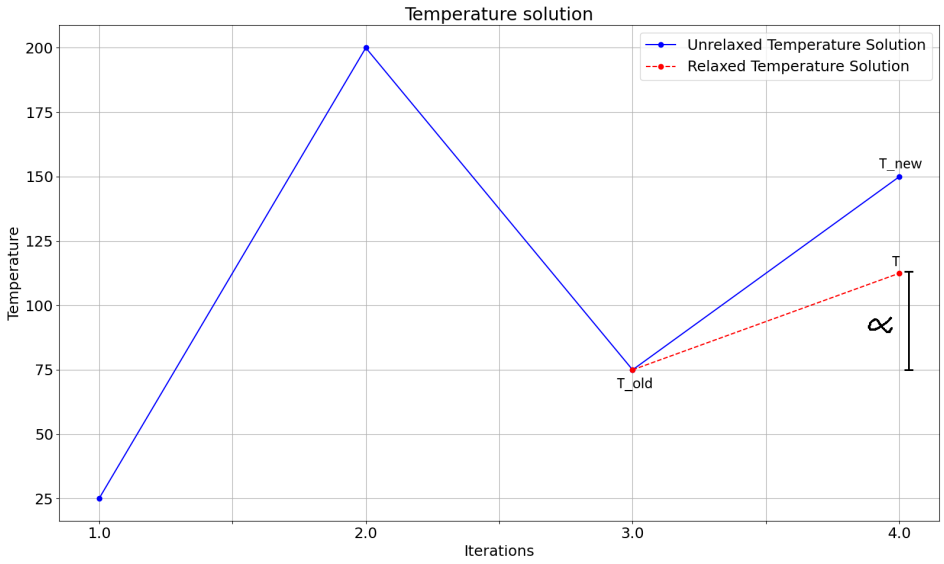

Figure 3.13: Representation of the relaxation factor

Once the solution converges, we have,

$$T_{new} = T_{old} \tag{3.2}$$

Substituting *Equation* 3.2 into 3.1, we see that $T = T_{old}$. The fraction used for relaxation is known as the *relaxation factor*, α. This value dictates how the updated value is calculated as,

Table 3.3: Relaxation factor usage

$\alpha < 1$	Under-relaxation, $T < T_{new}$
$\alpha > 1$	Over-relaxation, $T > T_{new}$
$\alpha = 1$	No relaxation, $T = T_{new}$

From table 3.3, we can visualize that a smaller α actually reduces the amount of oscillations in the solution, and therefore increasing system stability, although this comes at the cost of computing time, as the system would need more iterations to converge (as *change* between iterations is reduced). However, this can also lead to a *false convergence* scenario, that is, the solution appears to be stable, but if the number of iterations were to be increased, the solution would diverge. On the other hand, increasing α decreases the computation time, as the solution is brought to convergence quicker. Therefore, it is clear that choosing an appropriate value is a compromise between stability and speed. In this study, $\alpha = 1$ is what was found to be the value that provided a converged solution in reasonable time.

3.3.1.2 CFL Number

The *Courant-Friedrichs-Lewy* or *CFL* number, $\mathcal{C}$ is the ratio of the distance traveled by the fluid and length of the cell,

$$\mathcal{C} = \frac{Fluid\ distance}{Cell\ length} = \frac{\mathcal{U}\Delta t}{\Delta x} \tag{3.3}$$

In other words, the *CFL* number indicates how far the fluid travels in a given timestep. For example, a value of 0.3 and 1.1 means that, in a given timestep, the fluid has traveled 30% and 110% (across the entire length of the cell and a further 10%) throughout the cell, respectively. Looking at *Equation* 3.3, varying the CFL alters the time-step for the solution; it can help speed up the solution with higher values, where the fluid information can be communicated across multiple cells at once. A number of different values were explored with negligible change in the results (see *Figure* A.8) when the value was varied from $2-5$. The value used in this study is 4.

3.3.1.3 Weather File

The main input data for every simulation is the weather file. The days chosen for the temperature comparison are described with their parking directions in section 3.5. The file mainly contains the simulation duration ($0300 - 2000$ hrs), and the corresponding *solar irradiation, wind speed, wind direction, cloud cover* and *humidity*. In order to avoid excessively large data files, 3 measurements are made every 5 minutes. Furthermore, each measurement channel is recorded 3 times, with the *average, maximum* and *minimum* value. These values refer to the average, maximum and minimum values measured during the 5 minute window. In this study, for all comparisons with the measured data, the average values are used for comparison.

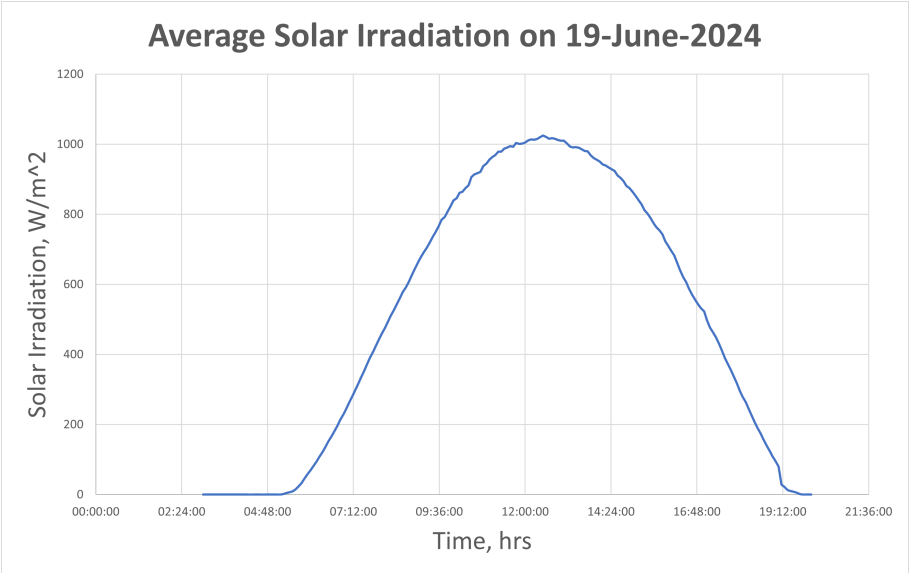

Figure 3.14: Average solar irradiation on $19 - June - 2024$

3.3.1.4 Radiation Patches

A radiation patch is a group of elements that are assigned a common-view factor to other radiation patches (see *Figure* 3.15). When the model is large, as in this study, these patches allow for a faster computation time of the thermal solution. The creation of these patches do not reduce the time taken to compute the view factors, as they are calculated for each element and then later averaged over the whole patch. These patches help reduce disk space needed to store these view factors. The exchange of radiation is done on a patch level when radiation patches are generated for a model such as in this study.

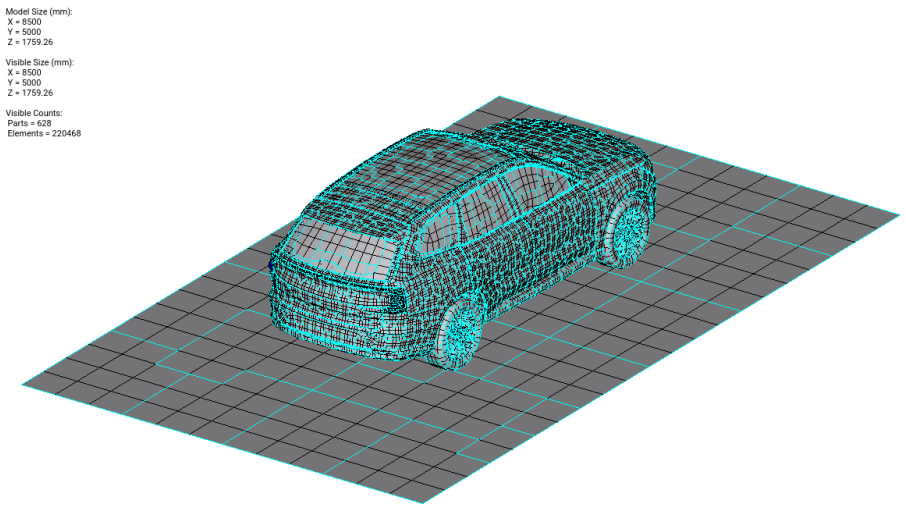

Figure 3.15: Radiation patches for the model

3.3.1.5 Multi-Grid Solver

Consider the energy equation to be solved to obtain a solution,

$$Ax = B \tag{3.4}$$

where x is the vector of unknowns; in this case they can be understood as the nodal temperatures of each element. As we know now, the iterations involve a degree of error across the solution process. If we look at the *spatial* error distributions between adjacent cells, we will encounter both *high* and *low* spatial frequency error distributions. The high frequencies are usually filtered out relatively easily after the first couple of iterations. It is the low frequencies that take quite some time to iron out on the way to a converged solution, and in turn increasing the computational time. The multi-grid solver, instead of storing the normalized error for each adjacent cell, it stores the values only for a couple of them, effectively "creating" a coarse mesh [7] . This, in a way, "transforms" the low frequency error distributions to high frequencies, which in turn can be removed with a few *Gauss-Siedel* iterations.

If we were to construct the low frequencies from the high frequency distributions using interpolation, the newly generated distribution would be a poor representation of reality due to *aliasing*. This is why it is important to already have a low frequency distribution (by *smoothening*) when moving between meshes, that is, from a fine to a coarse mesh. The *Multi-Grid* concept can therefore be outlined as [2],

- Perform a few iterations to remove the high frequency distribution
- Move to a coarse mesh
- Perform a few iterations to remove the low frequency distribution
- Move back to the fine mesh to perform the final few iterations and achieve convergence

To summarize the solver settings,

Table 3.4: Solver settings

Parameter	Value
Solver type	Multi-Grid method
Weather file duration	$0300 - 2000$ hrs
Time Step	10 mins
Relaxation factor, α	1
CFL number	4 (5 for *RapidFlow* with Wind)

3.3.2 Boundary Conditions

In a sun simulation model with $TAITherm$, there are no boundary conditions specified apart from the initial temperatures of the components, which is set to 20° C.

3.3.3 *RapidFlow*

The *RapidFlow* solver in *TAITherm* utilizes a $3-D$ fluid dynamics simulation model to solve for convection, as opposed to the $0-D$ lumped-capacitance model, where the temperature of the interior fluid is approximated to one value which is defined by a single fluid node. When *RapidFlow* is used, the position of this fluid node needs to be defined (blue sphere in *Figure* 3.16) such that the node lies within the fluid volume of the part inside convection is to be solved for.

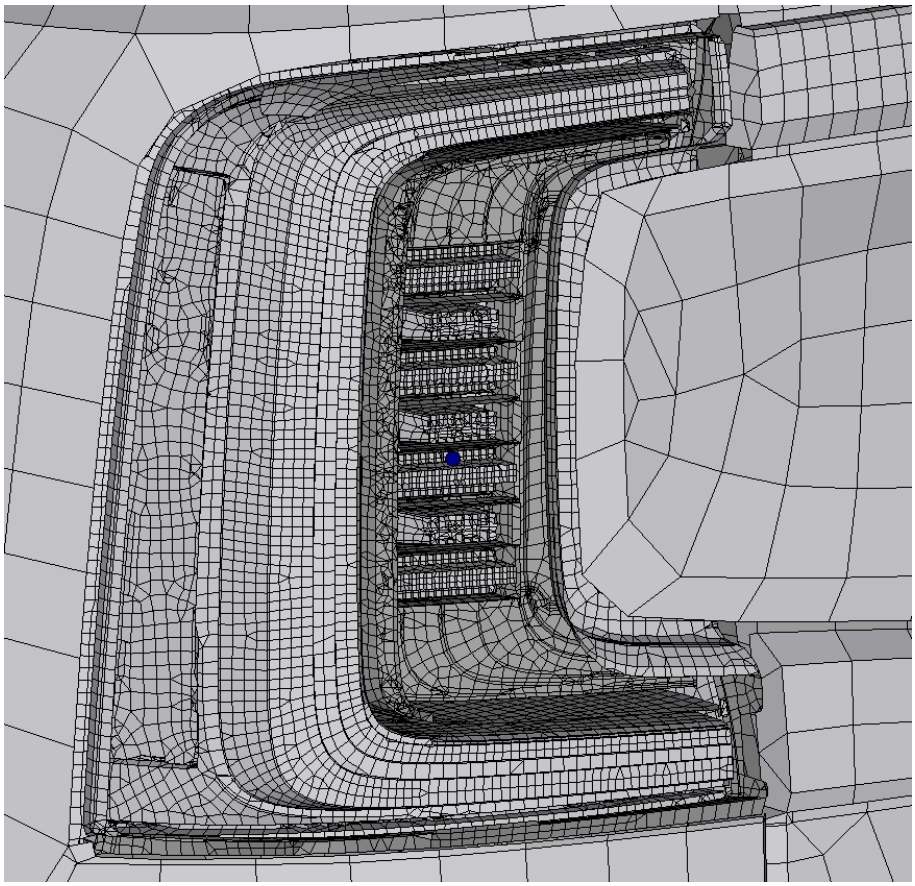

Figure 3.16: Fluid node representation

Based on the type of convection defined on each part surface, the fluid domain is formed using the initial fluid node placement. An error in this will result in the fluid volume "leaking", which simply means there is no geometry in the way to keep the air enclosed. A successfully created volume would look like that seen below, in *Figure* 3.17.

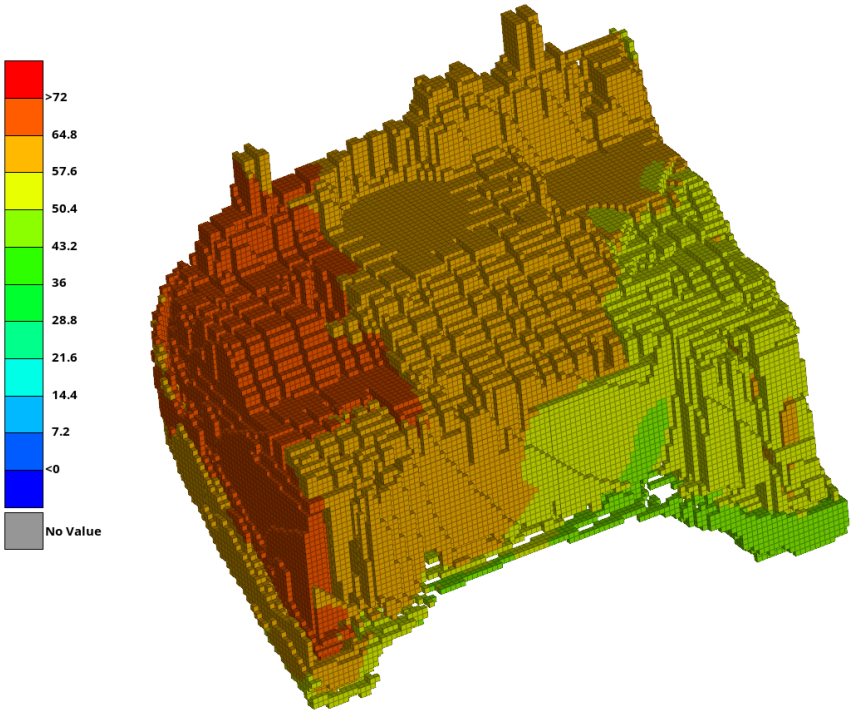

Figure 3.17: Temperature variation across the fluid volume

3.4 Post-processing

Post-processing is done using *META*. Here, the temperature gradient can be seen on the lamp in different time steps, as seen in *Figure* 3.18.

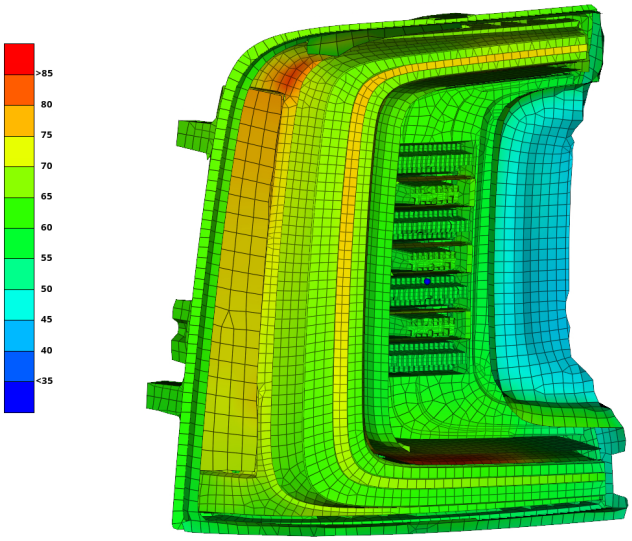

Figure 3.18: Surface temperature gradient

This is done once we have the results available from *TAITherm*. These contour plots will look different for different parking directions. Therefore, we will be able to collect data on not only the point/area of maximum temperature, but also the

heading when it occurs. It is also beneficial to know for how long this temperature lasts in the region, and this will also be considered as part of this study.

3.5 Case Studies

The project plan described thus far will be performed for a few test cases. The differentiating factors would be the wind, heat source inside the lamp, and the correlations on different days,

1. **Stable solar irradiation:** 19−June−2024 with a 315° parking direction. This day was chosen due to smooth variation in solar irradiation across the day, indicating minimal affect of cloud cover.

2. **Hottest day:** 05−July−2024, with 315° parking direction. This is the day when the ambient temperature is the highest.

3. **Hottest part temperature:** 03−August−2024, with 0° parking direction. This is when the surface temperature of the second thermocouple is the highest. This thermocouple is chosen as it reaches the highest temperature when compared to the other three interior thermocouples.

4. **Car is turned on:** Here we run the same simulation but also include the light bulb in the lamp as a heat source in order to replicate the scenario when the car is turned on.

4

Results

Two main parameters were chosen to start with when comparing the temperature accuracy between iterations.

- **White tape thermocouple**: Measurement of the maximum thermocouple temperature present on the lens surface, fastened using white tape, as shown in Figure 4.1.
- **Interior thermocouples**: Apart from the one with the white tape, there are four more thermocouples (see *Figure* 4.2) whose temperature readings are compared against the simulated data.

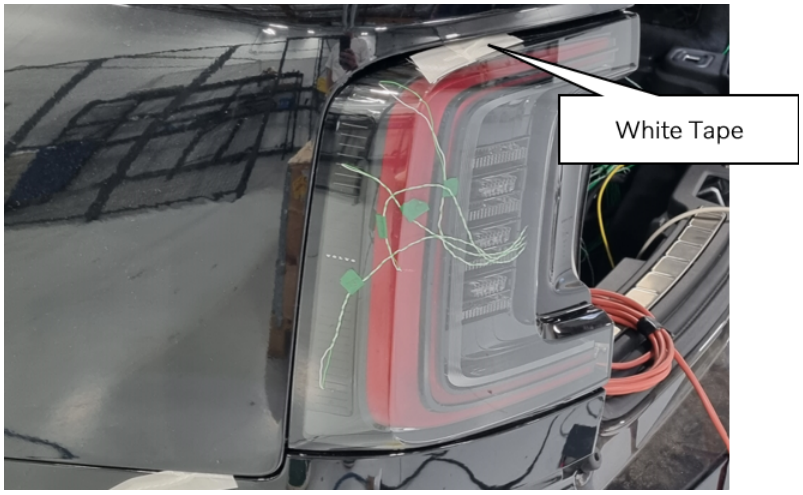

Figure 4.1: Thermocouple kept in place by a white tape

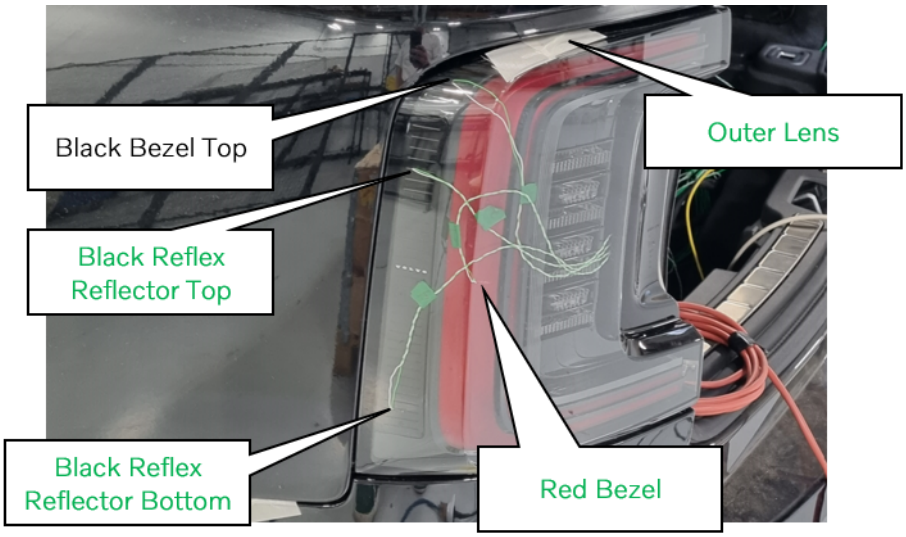

Figure 4.2: Interior thermocouples in the left rear lamp

The thermocouples in *Figure* 4.2 that are highlighted in green indicate that these lie on transparent or IR transparent materials.

4.1 Need for *RapidFlow*

Using the *RapidFlow* solver significantly increases the computational time since there is a need to create fluid meshes. Depending on the size of the volume and the corresponding fluid cell size, the run time increases further. Therefore, it is essential to know the difference in accuracy between the two methods. *Figure* 4.3 shows the difference maximum and minimum element temperatures within the fluid volume. It is seen that they differ by almost $30°C$.

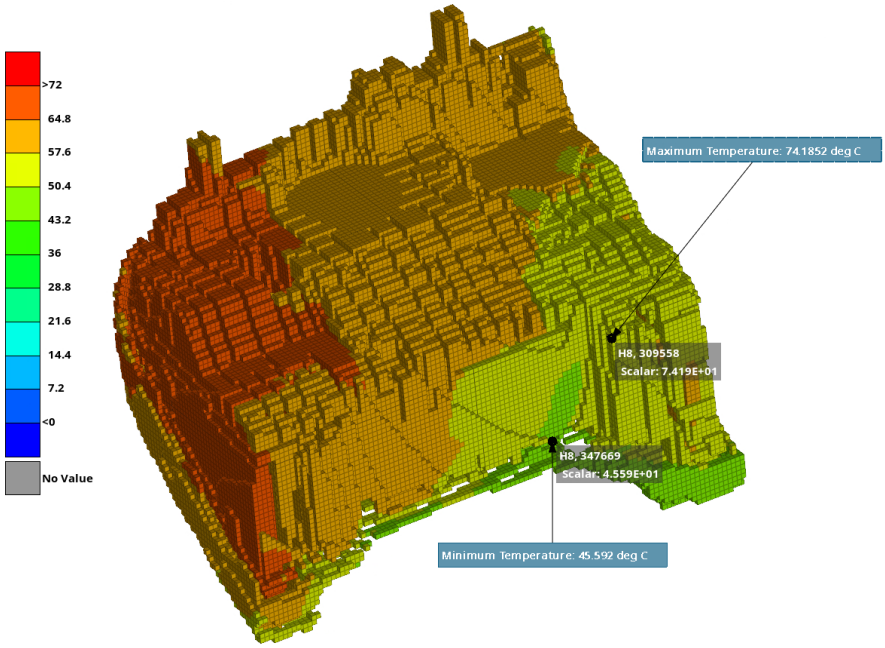

Figure 4.3: Difference in minimum and maximum air temperatures across the fluid volume

Figure 4.4 shows the temperature variation across the day for the minimum (orange curve) and maximum elements (blue curve), along with the results from the $0-D$ lumped capacitance model (*i.e.*, without *RapidFlow*, green curve).

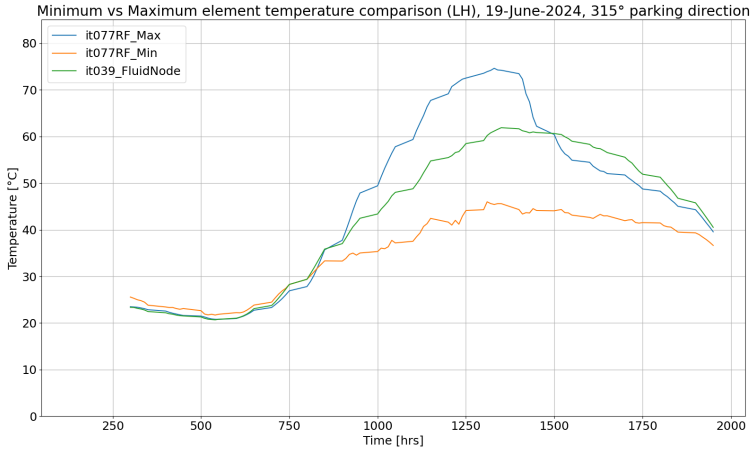

Figure 4.4: Comparison between minimum, maximum and fluid node temperatures

We see this model results in an approximately median solution between the extreme values. This can be useful for quick checks for model and material validation, however, this is not a very accurate representation of the temperatures. The thermocouple temperature variations are depicted by the *Figures* 4.5, 4.6 and 4.7,

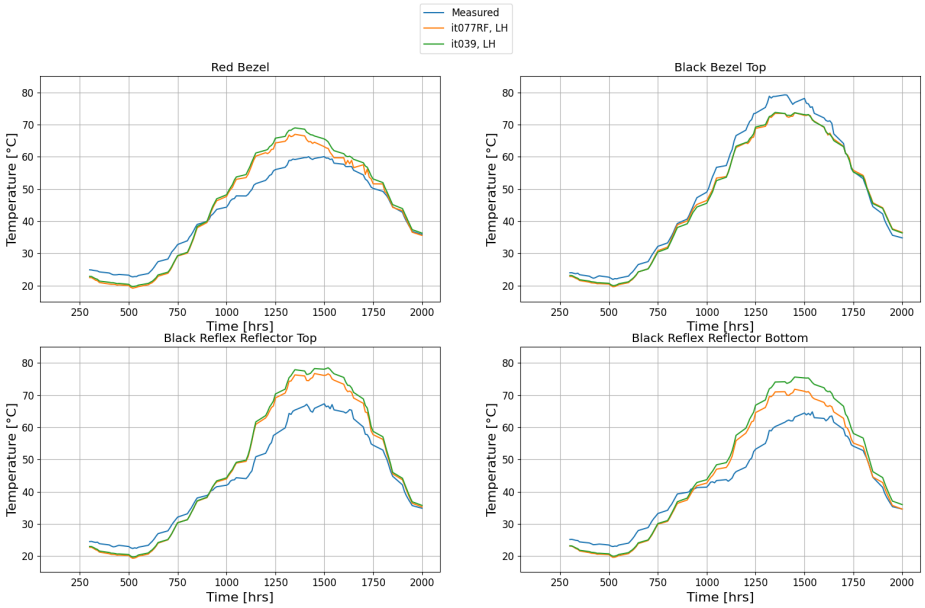

Figure 4.5: Left Rear Lamp (With [*it077RF*] and without *RapidFlow* [*it039*])

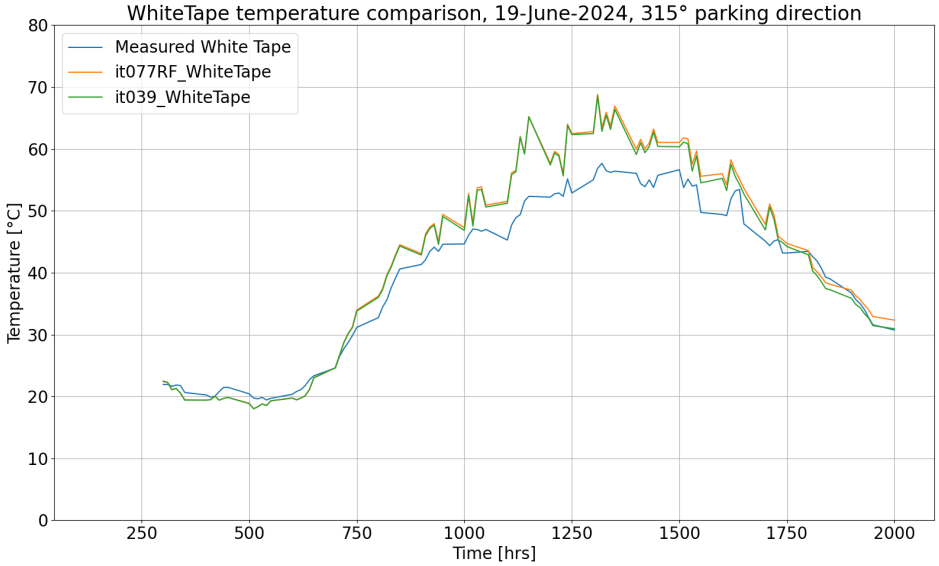

Figure 4.6: White Tape thermocouple (With [*it077RF*] and without *RapidFlow* [*it039*])

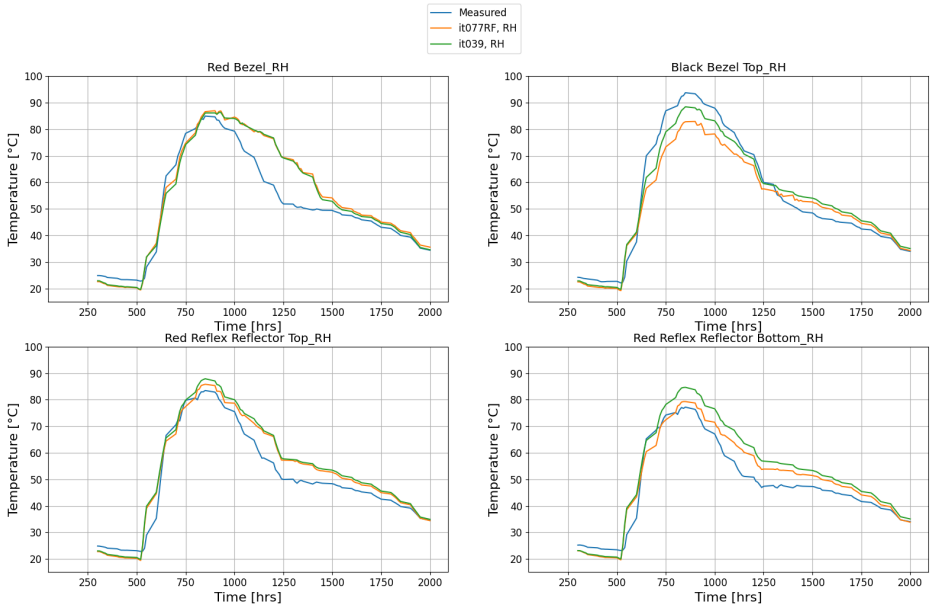

Figure 4.7: Right Rear Lamp (With [*it077RF*] and without *RapidFlow* [*it039*])

It is clear that there is a slightly larger delta when the *RapidFlow* solver is not used, indicated via an over-prediction. This was expected, as the temperature of an individual fluid node used to represent the interior temperature would not be as accurate as creating a fluid mesh where one can select individual elements to evaluate the temperature variation at that point. This over-prediction is minimal on the white tape thermocouple in *Figure* 4.6 as it is on the outside and therefore would not depend as much on the interior temperatures.

4.2 Using *RapidFlow*

The measurements made by the thermocouples can either be the air temperature inside the lamp or the surface temperatures of the parts. Upon closer inspection of the samples used for the physical testing (see *Figure* 4.8), it was clear that the thermocouples were melted into the surface of the components, indicating that they measure surface temperatures. This section evaluates the variation for Case 1 from *Section* 3.5.

Figure 4.8: Closer look at the first and fourth thermocouple inside the lamp, respectively

Figure 4.9 shows the variation of the surface temperatures of the interior thermocouples of the left lamp. The *"Black Bezel Top"* thermocouple has the best correlation, matching the measured curve very well. This is because this is the only thermocouple in this study that lies on a non-transparent surface. This was also one of the parts for which the surface properties were also measured as described in *Section* 3.1.

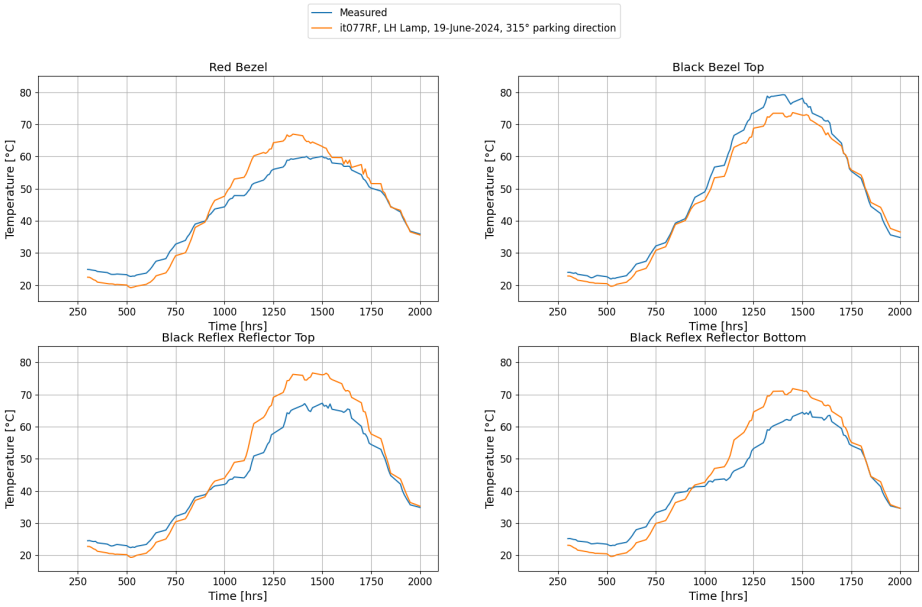

Figure 4.9: Left rear lamp temperature comparison

The thermocouple under the white tape, measured and illustrated in *Figure* 4.10, also does not deviate too much from the measured values.

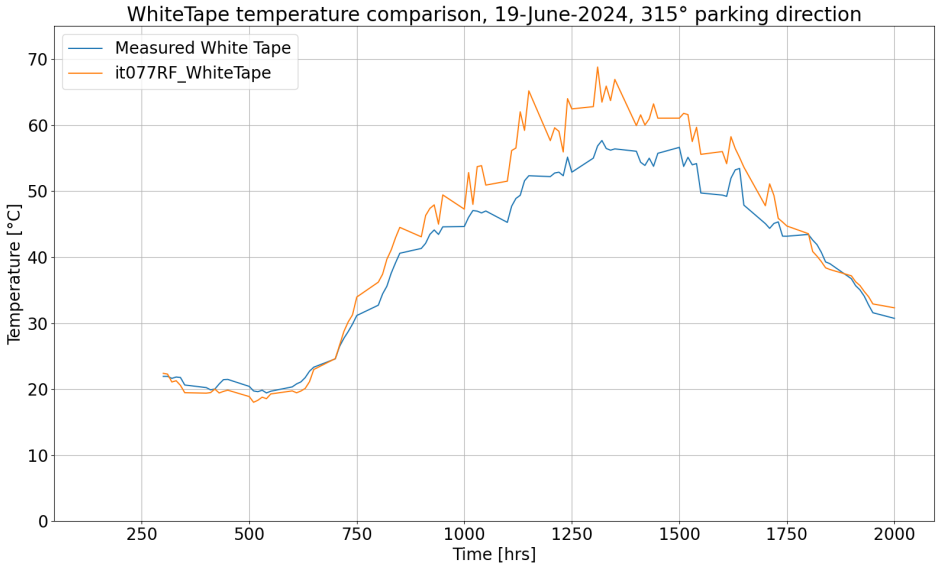

Figure 4.10: White tape temperature comparison (Left lamp)

The assembly was mirrored to simulate the rear lamp on the right side. This is because in the vehicle on the proving ground, the reflex reflector is made up of a different material ($PMMA$) and also has a different color (*red*, see *Figure* 3.5) compared to the left (*Polycarbonate*, *Black IR Transparent*, see *Figure* 4.11).

Figure 4.11: Black IR transparent reflex reflector on the left lamp

The variation of the thermocouple temperatures in the right lamp, as seen in *Figure* 4.12 shows a good correlation, especially at the peaks. This is likely because for this

parking direction (315°), the right lamp is more exposed to the sun. This means that solar irradiation has a greater influence on the temperature variation compared to surface-to-surface radiation, which is discussed in further detail in *Section* 5.4.

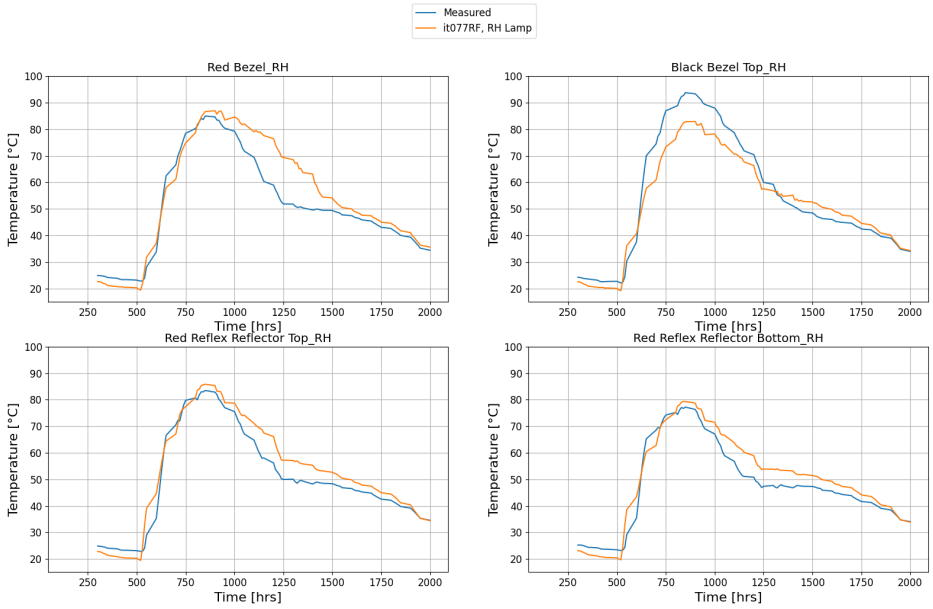

Figure 4.12: Right rear lamp temperature comparison

To take into account the *IR transparent* nature of the black reflex reflector, the transmittance and reflectance curve obtained from the supplier were used, and from these curves it was clear that the wavelength of light passing through the reflector falls in the *IR* spectrum. In all the other spectral ranges, the transmitivity would be understood to be negligible.

4.2.1 Hottest day

From the master weather file, the day when the ambient temperature was found to be the highest was identified as $05 - July - 2024$. For this day, the parking direction was the same (315°) as the day used for the baseline analysis in this study, as mentioned in *Section* 3.3.1.3. The correlation for the second thermocouple is much better in comparison to the others; it mimics the nature of the measured curve quite accurately. The other three simulated thermocouple temperatures are once again slightly on the higher side, although the deltas at the peak are slightly smaller compared to *Figure* 4.9.

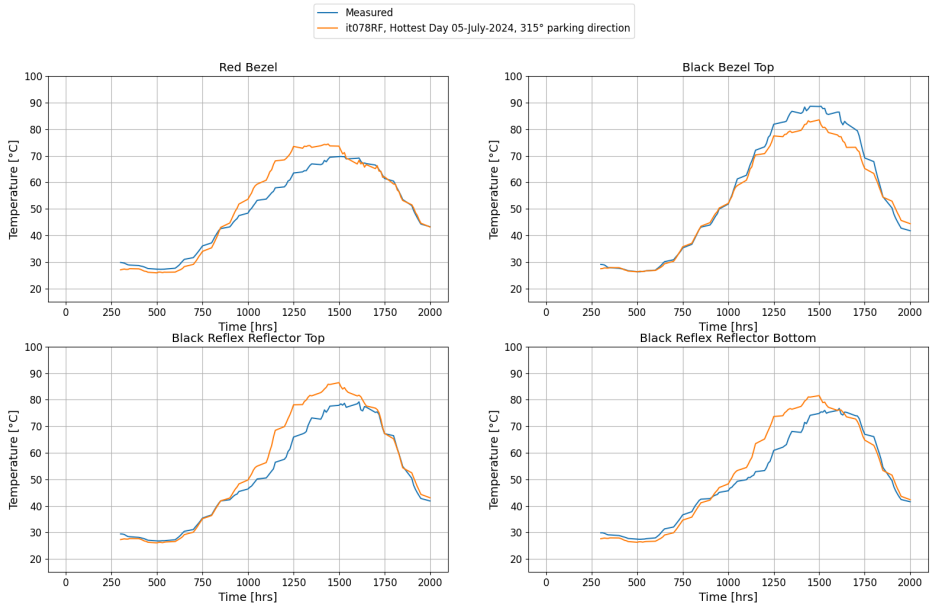

Figure 4.13: Temperature comparison for the hottest day, left rear lamp

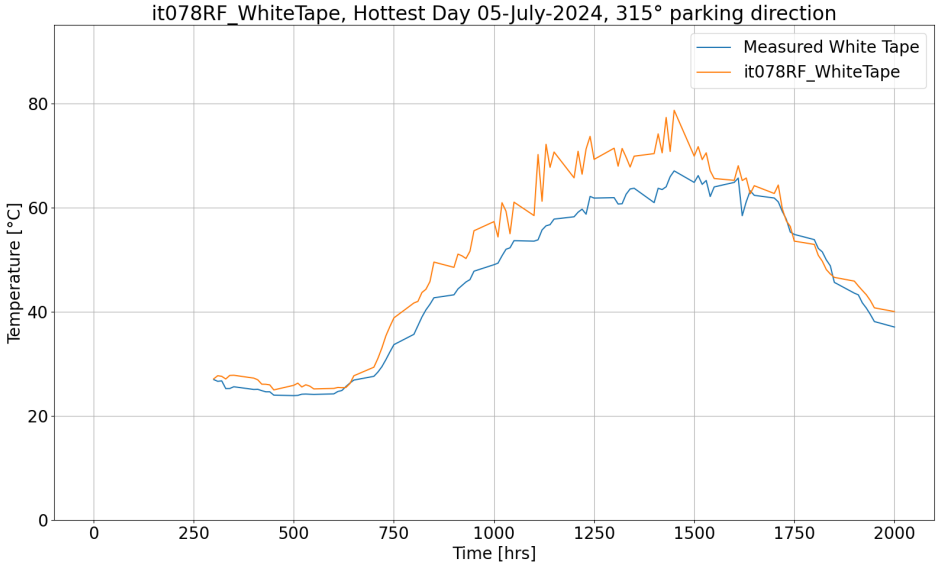

Figure 4.14: Tape temperature comparison for the hottest day, left rear lamp

4.2.2 Hottest part temperature

As mentioned in *Section* 3.5, $03-August-2024$ was the day when the *Black Bezel Top* thermocouple reached its highest temperature. The car was parked with a 0° parking direction. *Figures* 4.15 and 4.16 show a good correlation between the measured and simulated temperatures, however, approximately between $16:20 - 17:40$ there is

an offset in the measured values when the thermocouple cools down after the peak temperature. This is discussed further in *Section* 5.2.

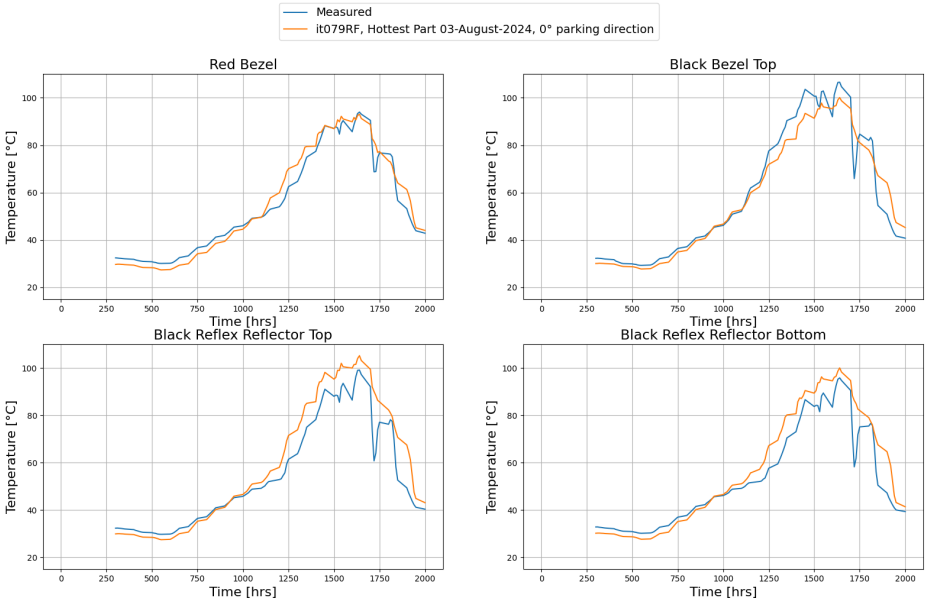

Figure 4.15: Temperature comparison for the day when thermocouple *Black Bezel Top* has the highest temperature, left rear lamp

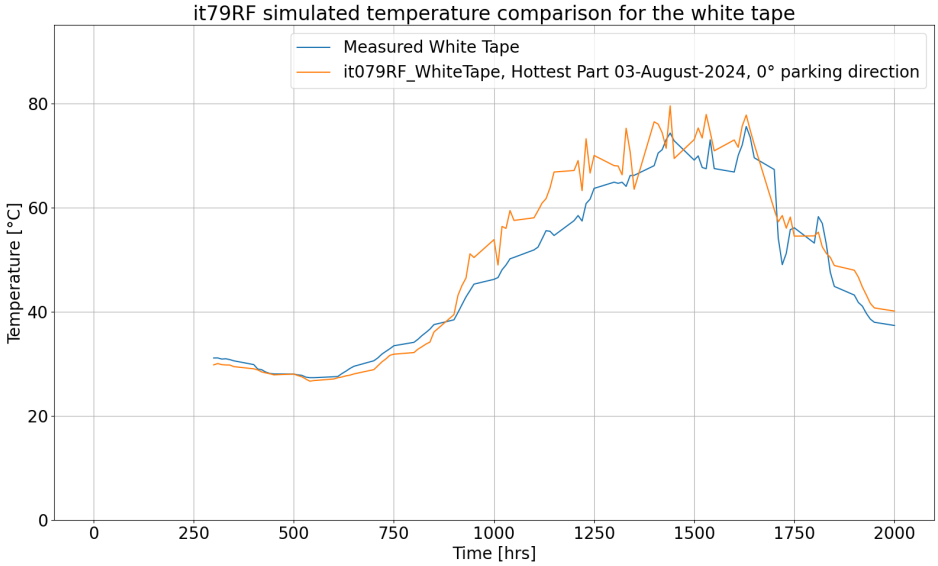

Figure 4.16: Tape temperature comparison on $03 - August - 2028$, left rear lamp

4.3 Using *RapidFlow*, with Wind

A wind flow simulation using *TAITherm* provided the opportunity to simulate the wind flow, and the resulting convection effects it can have on the parts it encounters when moving around the vehicle using $3-D$ fluid dynamics, as opposed to the conventional $0-D$ wind convection correlations that are used in the previous sections that only consider ambient wind speed. The weather file, as explained in *Section* 3.3.1.3, contained the wind speed and direction data. These values will be used to set boundary conditions at the "ambient" boundaries, which are created automatically based on the extents of the domain. The dimensions of the domain are a combination of the model geometry size, as well as any additional padding parameters provided in the solver configuration file.

$$h = C_1 + C_2 V \tag{4.1}$$

where, C_1 and C_2 are coefficients. Equation 4.2 shows a linear convection coefficient equation which is utilized when the $0-D$ wind convection model is selected.

When a $3-D$ model is used for the wind instead, the following equations are used to determine the heat transfer coefficient,

$$h_{nat} = 1.52(\Delta T)^{\frac{1}{3}} \tag{4.2}$$

$$h_{for} = 7.1(U)^{0.78} \tag{4.3}$$

$$h = (h_{nat}^6 + h_{for}^6)^{\frac{1}{6}} \tag{4.4}$$

The heat transfer coefficient accounts for both natural and forced convection.

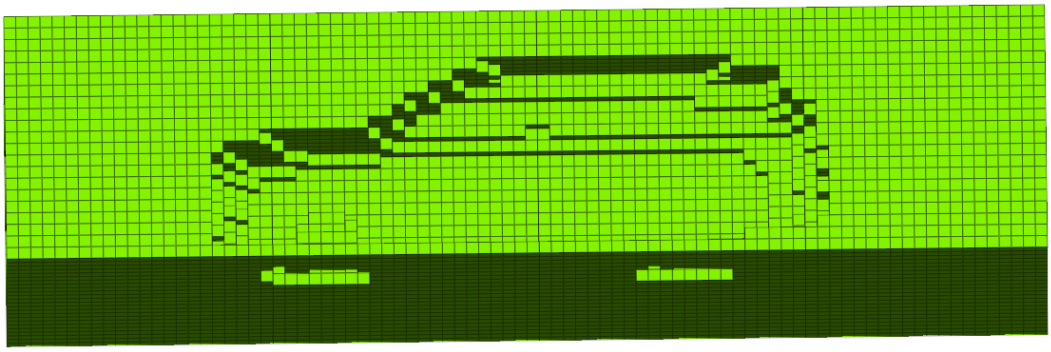

Figure 4.17: Fluid domain of the wind

The fluid domain for the wind had a cell size of 100 mm. This is due to the size of the domain itself, and having smaller fluid cell sizes would mean the number of

fluid cells would be much higher, therefore leading to higher computational time and power. *Figure* 4.17 shows a section view of the wind fluid domain across the vehicle. In the x (along the length of the vehicle) and y (across the vehicle) directions, no padding has been added as the wind boundary would be decided by the extent to which the gruond extends in these directions. However, in the z direction, a padding of 4 cells or 400 mm is added so that sufficient effect of the wind flowing over the hood is also taken into account.

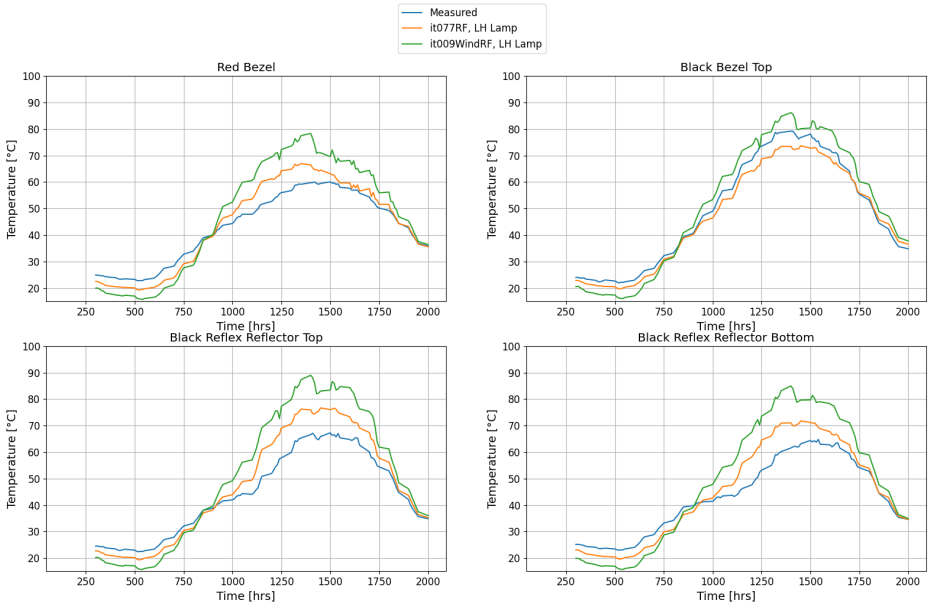

Figure 4.18: Thermocouple temperature comparison when *RapidFlow* is used for the wind, left rear lamp (*Case* 1 from 3.5)

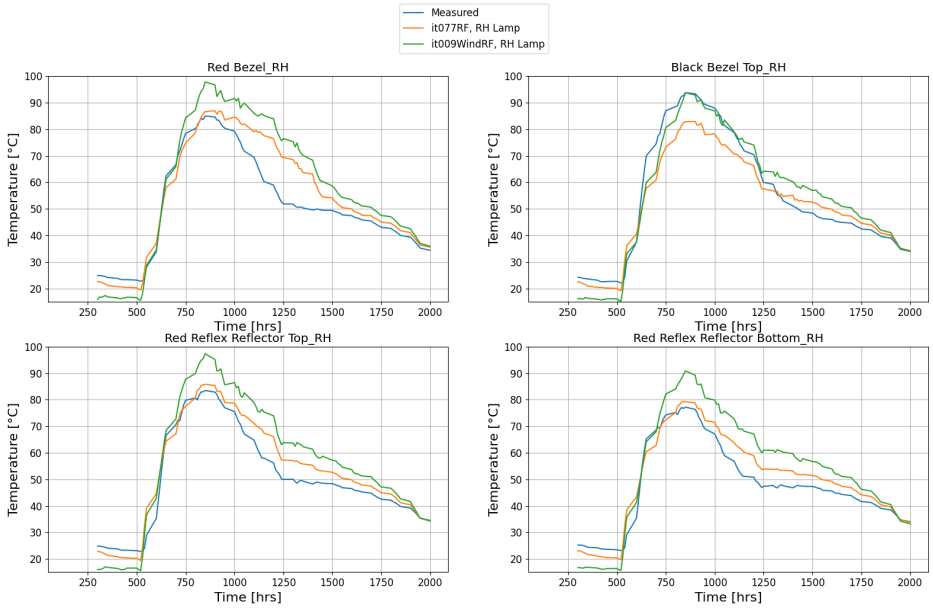

Figure 4.19: Thermocouple temperature comparison when *RapidFlow* is used for the wind, right rear lamp

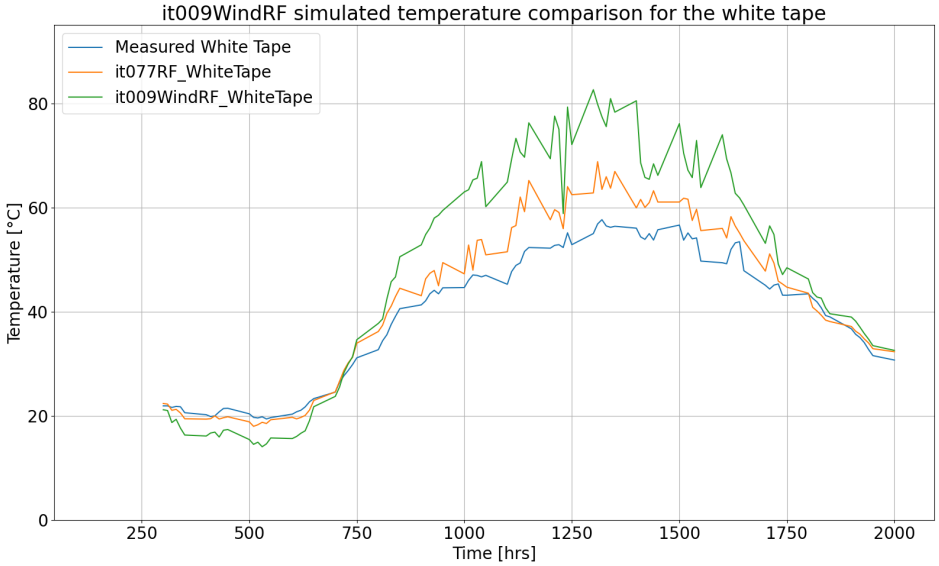

Figure 4.20: White tape thermocouple temperature comparison when *RapidFlow* is used for the wind, left rear lamp

As is evident from the *Figures* 4.18, 4.19 and 4.20, the simulated temperatures for the case where *RapidFlow* is used for the wind domain are also higher than when it is not used. This can be attributed to the fact that depending on the direction of the wind and where it hits the vehicle, there will be a recirculation zone (see *Section* 2.3) on the other other side of the body, implying that in this region there will be

significantly lesser wind and therefore providing both the left- and right-hand side rear lamps with minimal cooling and hence increasing their temperatures.

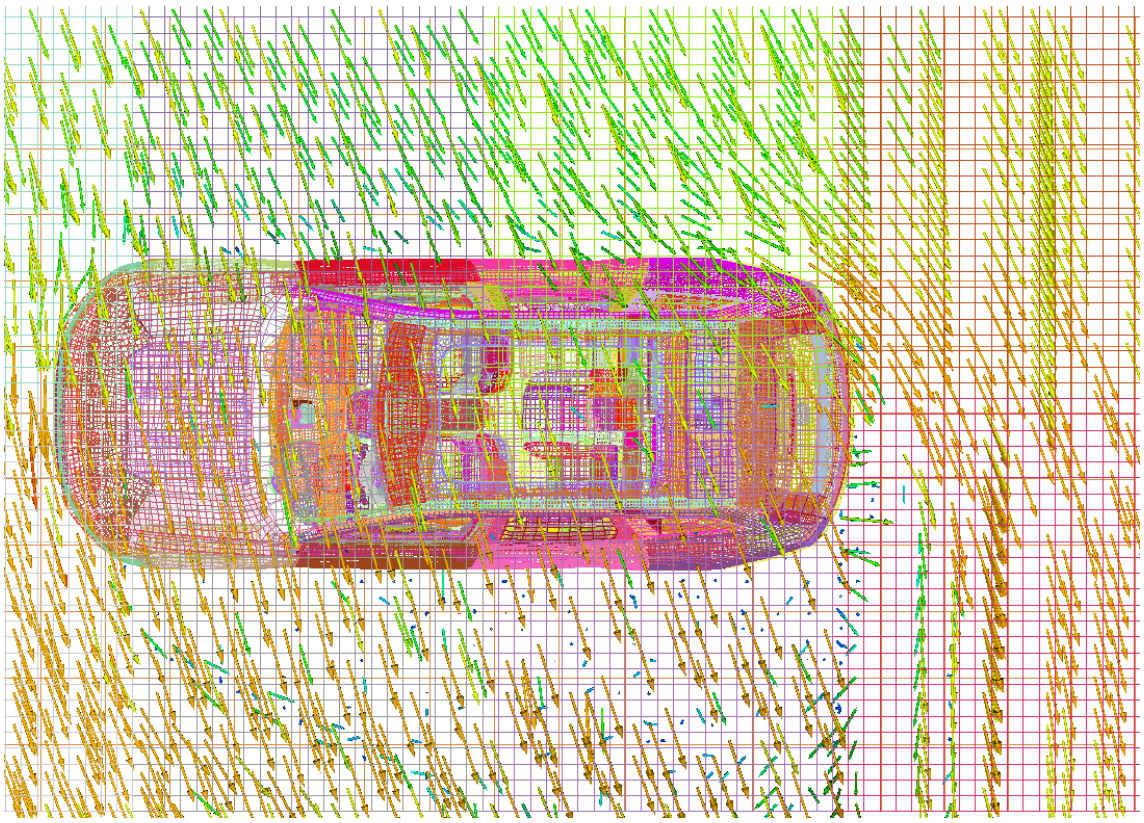

Figure 4.21: Velocity vectors around the vehicle at a given time step

Figure 4.21 shows the wind direction and speed in the form of velocity vectors; the wind speed is scaled with the lengths of these vectors, and the direction with where the vectors point. We can see that when the wind hits the vehicle in front, there is a slight dip in wind speed before moving along the sides with sufficient velocity. However, the rear of the vehicle shows significantly lesser wind speed and with vectors pointing in multiple directions, indicating that a region of recirculation is present.

4.4 Wind Speed Comparison

In an attempt to further understand the deviation of the simulated temperatures from the measured values, the wind speeds measured by the stations surrounding the car (see *Figure* 4.22), as well as the top station, were compared with the speeds obtained from the simulations.

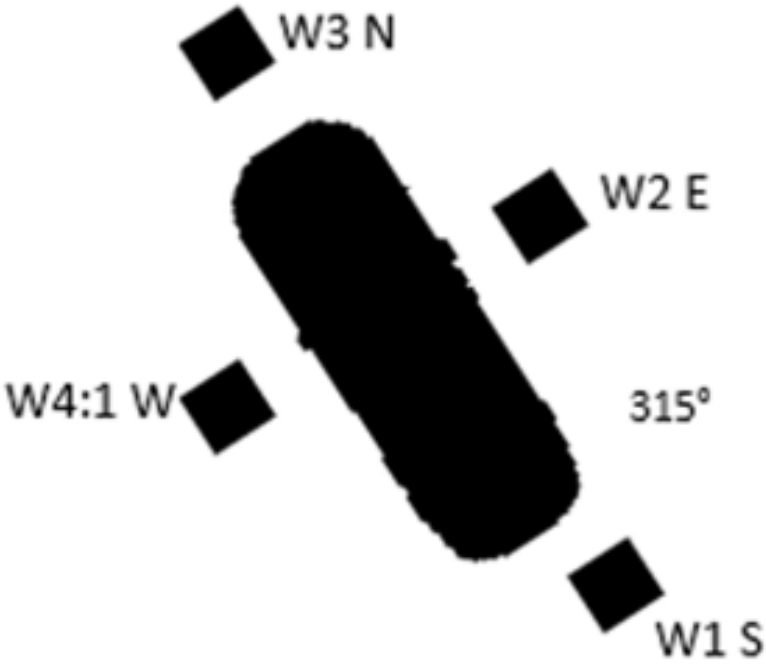

Figure 4.22: Wind speed positions around the car

Figure 4.23 shows a comparison between the wind speeds across different wind domain sizes. In the plots, the *orange* curves represent a domain with a 4 cell padding in only the z direction, and the *green* curves represent a domain with a 4 cell padding in all directions.

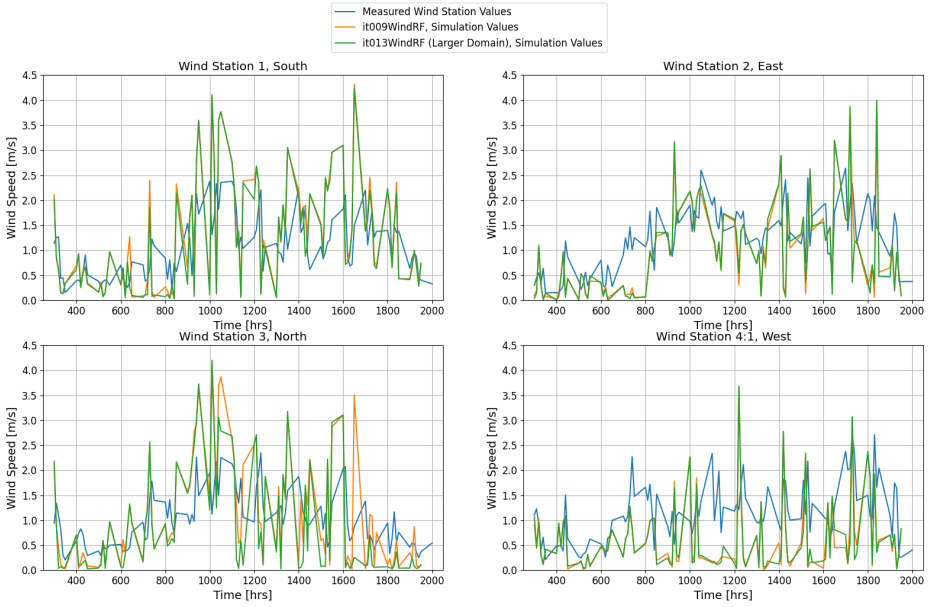

Figure 4.23: Wind speed comparison around the car

On the other hand, for the wind station above the car (see *Figure* 4.24), the results correlate significantly better with the measured values, see *Figure* 4.25.

Figure 4.24: Wind station on top of the car

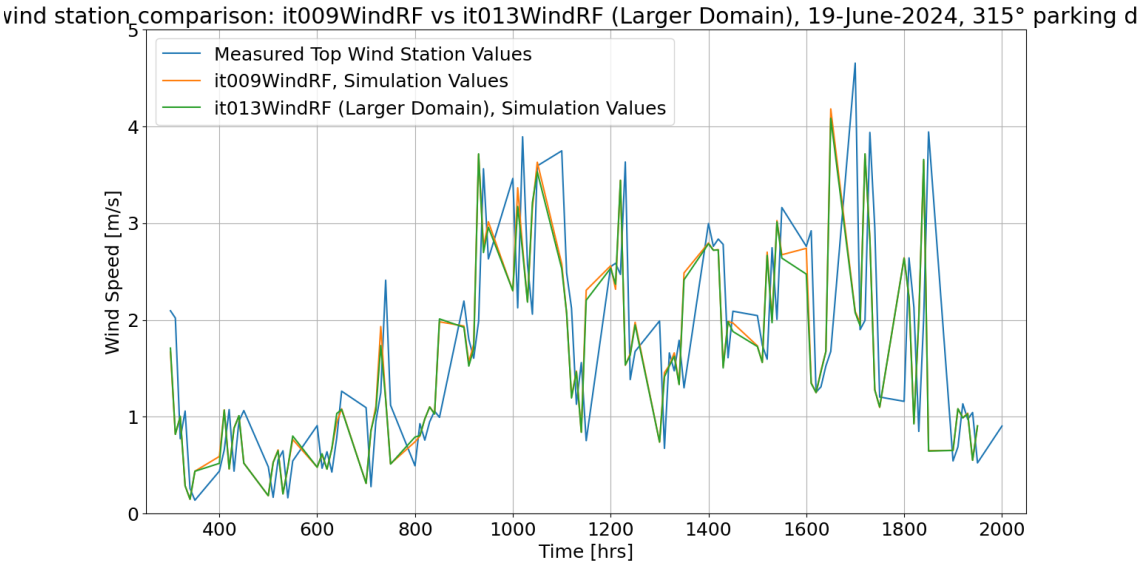

Figure 4.25: Wind speed comparison on top of the car

This poor correlation (for the wind stations surrounding the car) can also be seen as a contributor to the error in the *RapidFlow* wind model (see *Section* 5.1.2).

4.5 Aerodynamics Correlation

To validate whether the wind speeds from the simulations are representative of real-world conditions, point cloud data from a CFD simulation were obtained for the Volvo $C40$. The objective was to compare the velocity values at different points around the car, with those obtained via the solver.

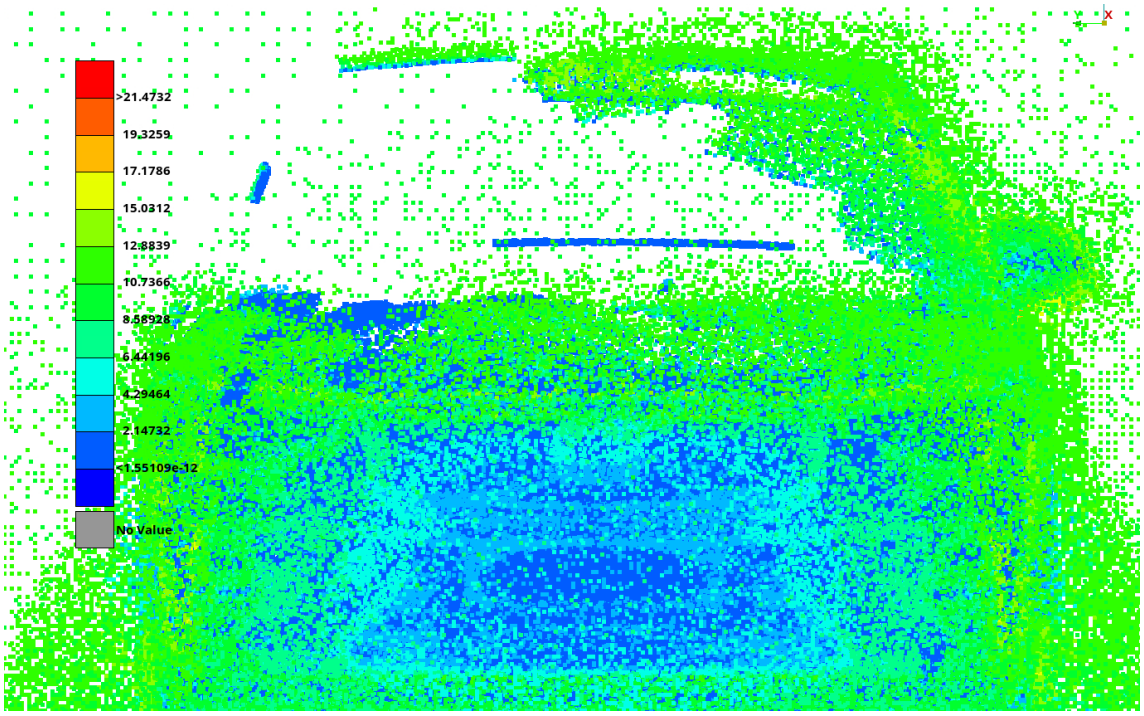

Figure 4.26: Point Cloud Data from wind tunnel testing

Table 4.1: Wind speed comparison with point cloud data

Location	**Simulation** (m/s)	**Wind Tunnel** (m/s)
Front	1.245	1.281
Left Tire	0.1489	1.5147
Right Tire	0.2507	1.6480
Above	2.301	3.729

This difference in magnitude can be attributed to the fact that the fluid cell size is 100 mm, selecting data points a little further away from the surface may give a better correlation. In addition to this, human error in selection would always be involved.

5
Conclusion

From almost all the simulations run so far, it is seen that the correlation gets better when the lamp is more exposed to the sun. This is further re-instated by the results obtained from the hot day and hot part, where the correlations, especially at the peak, are quite good.

5.1 Over prediction

5.1.1 Starting temperature

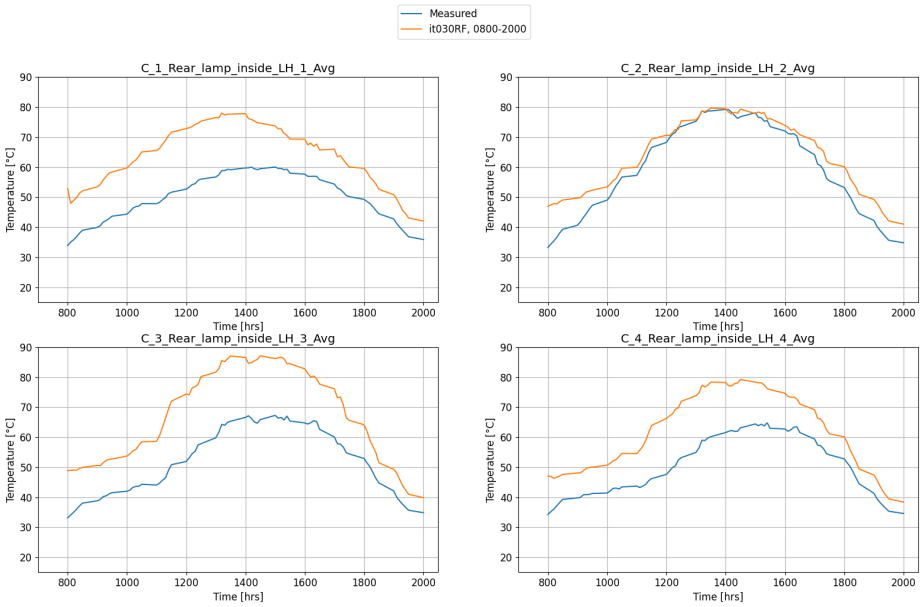

Figure 5.1: 0800 – 2000 as the run time period

After the initial results were obtained, the starting temperature (see *Figure* 5.1) is approximately 50°. This does not seem to be physical, especially because the ambient temperature at that point in time is between 25°−30°, and there is very little solar radiation that impinges on the lamp. The weather file was modified to start the solver from 0300 instead, because at this timestep, it is ensured that there is zero solar flux on the lamp. *Figure* 4.9 shows the new temperature variation, with an accurate starting temperature.

5.1.2 Relative Errors

In order to quickly understand what type of simulation has the best comparison to the measured temperature variation, the relative errors for each of them are plotted in *Figure* 5.2.

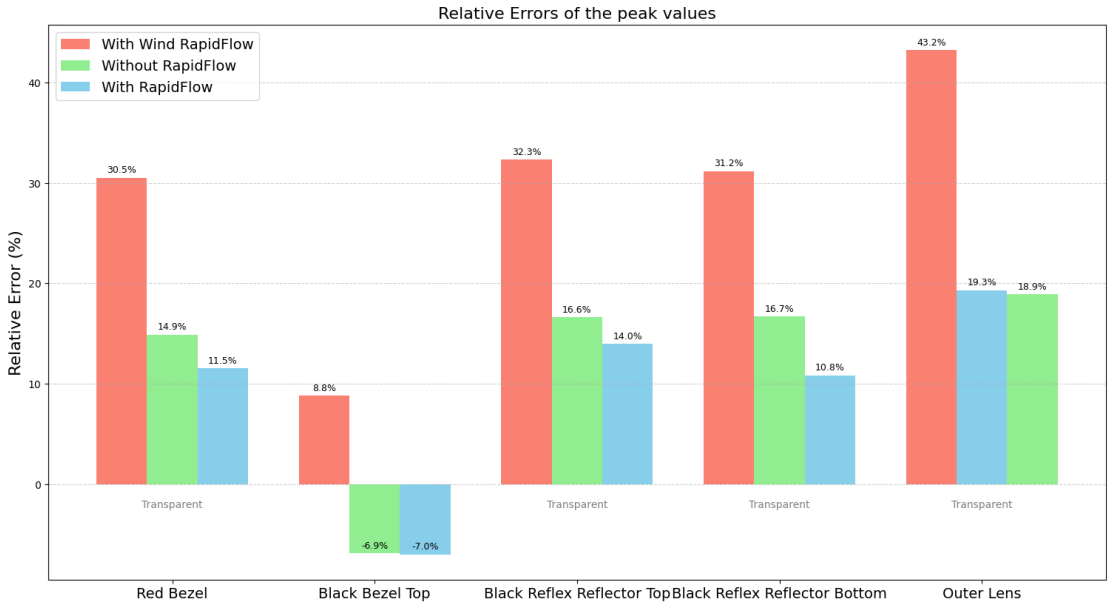

Figure 5.2: Error comparison between simulation types

It is clear that using *RapidFlow* for the wind generates the highest error, whereas when it is not used, the error is the least. However, this would not be physical as the vehicle would most definitely be affected by the wind surrounding it. It is also worth noting that the thermocouples with comparatively higher error percentages are those that lie on transparent or *IR* transparent parts (see *Section* 5.4).

5.2 Offset in prediction

As mentioned in *Section* 4.2.2, there is a slight offset in when the peak temperatures starts declining due to cooling (see *Figure* 4.15) before heating up once again to reach its second peak.

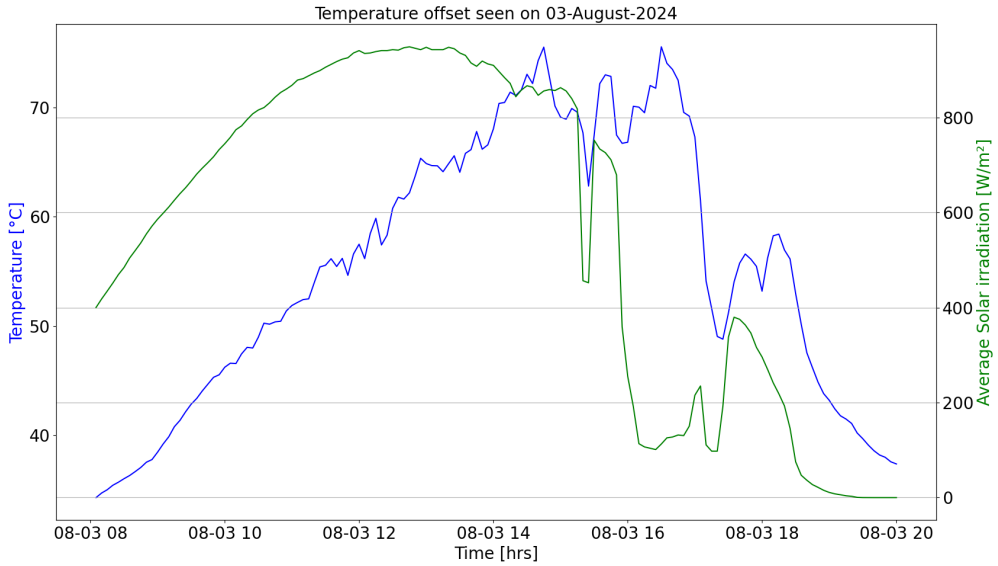

Figure 5.3: Delay in temperature drop after peak

Figure 5.3 illustrates the offset from a solar irradiation stand point. The blue curve represents the *Outer Lens* thermocouple, and the green curve represents the average solar irradiation on the day $(03 - August - 2024)$, between $0800 - 2000\ hrs$. From the solar radiation curve, we see that approximately between $1550 - 1600\ hrs$, there is a drop. However, the temperature drop occurs only after about $45\ mins - 1\ hr$. This could be because of localized clouds, for example one vehicle on the proving ground is affected by this and not another vehicle that is perhaps $5 - 10\ m$ away. During the day, this can also occur due to "dark spots" caused by floodlights (see *Figure* 5.4), that create a local shadow affecting one or multiple parts.

Figure 5.4: Localized dark spots caused by a floodlight at the proving ground

5.3 Computation time

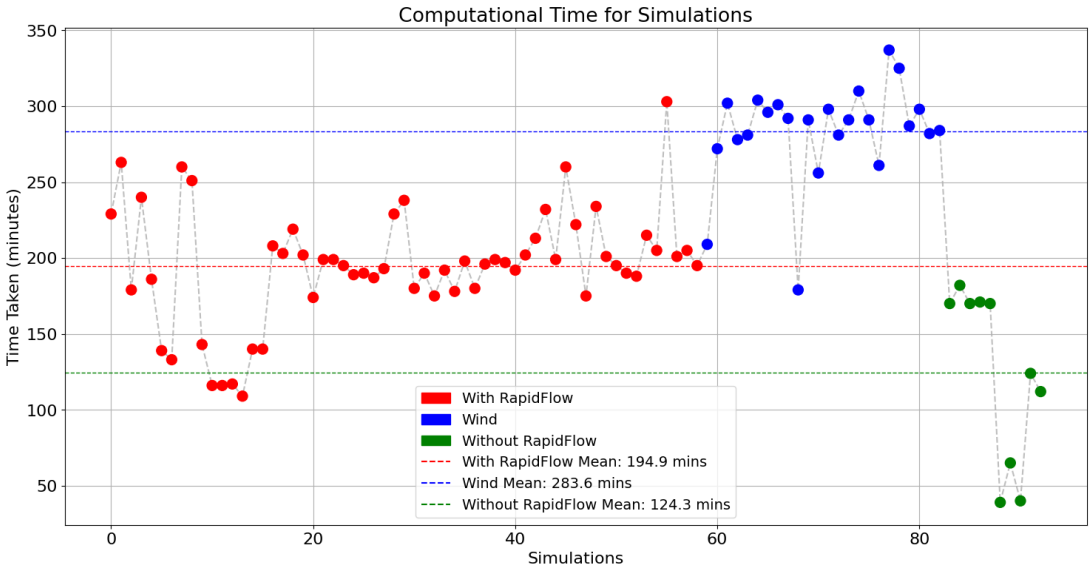

Figure 5.5: Difference in the computational runtime between the different types of simulations run in this study

Figure 5.5 shows a brief overview of the different types of simulations run in this study, categorised by the convection model used and for which fluid domain. The findings are also summarised below in Table 5.1.

- Red - These data points indicate that the convection heat transfer for the fluid domain within the rear lamp is solved using a $3-D$ fluid dynamics model (*RapidFlow*).
- Blue - In these simulations, the $3-D$ model is extended to the wind domain.
- Green - A $0-D$ lumped capacitance model is used where the interior fluid temperatures are approximated to one fluid node (no *RapidFlow*).

The dashed horizontal lines show the average time taken by the simulations in each set. The least amount of time is taken when *RapidFlow* is not used and therefore the interior fluid temperature is approximated to one fluid node. The average time for each simulation in this case would be much shorter (around 50 $mins$) than the mean value of approximately 2 hrs 6 $mins$, however, in the 2025 version these simulations started taking a lot longer when compared to the 2024 version (notice the 3 data points in the bottom right).

The next set of simulations involved using independent fluid nodes for each of the lamps, and using $3-D$ fluid dynamics model to solve for the convective heat transfer. The variation between these simulations stems from the differences in versions, CFL numbers used, and matrix update frequencies among other solver settings. This translates to an average runtime of approximately 3 hrs 9 $mins$.

It is clear that when the $3-D$ model is extended to the wind, the simulation takes a little longer to run, with an average runtime of approximately 275 $mins$ or 4 hrs 35 $mins$. This is because these types of simulations typically contain 3 independent fluid domains, one for each lamp, and one for the wind.

Table 5.1: Simulation runtime comparison

Simulation	**Number of Fluid nodes**	**Average runtime**
No *RapidFlow*	1 ($0-D$ lumped capacitance model)	2 hrs 6 $mins$
With *RapidFlow*	2 fluid nodes ($3-D$ fluid dynamics model)	3 hrs 9 $mins$
RapidFlow on wind	3 fluid nodes, including the wind domain	4 hrs 35 $mins$

5.4 Surface-to-Surface radiation

Surfaces that follow Kirchhoff's law (see *Section* 2.5) equate emissivity with absorptivity. However, $TAITherm$ treats these two independently, since they operate in different wavebands and thus refers to absorptivity as the *solar absorptivity* and the

surface-to-surface radiation wavebands are represented by the emissivity. This means that the transparency curves defined for a part will only be representative of the solar radiation. This is further validated by the deltas seen between the measured and simulated temperatures of the thermocouples lying on transparent surfaces. The curve implies that the part is transparent primarily to the solar irradiation in this region, and not the surface-to-surface radiation. This will result in all this radiation being absorbed by the parts, and hence leading to an increase in the temperature.

One way to mitigate this effect is to calibrate the emissivity value, where we can decide how much energy a part can dissipate, therefore having an effect on its surface temperature.

5.5 Recommendations

Based on the limitations and the results obtained, the following proposals can be made,

- **Transparent parts**: Throughout this study, it has been quite difficult to get a good correlation for the transparent parts. We have seen that the surface-to-surface radiation plays a crucial role in defining the surface properties of the parts, and therefore, it is imperative that a good method is devised to counter this. For example, varying the emissivity can help regulate how much energy is absorbed/given off by a surface.

- **Wind Model**: In this study, the universal wind model was used. However, in an attempt to reduce the error deviation, another wind model was explored (see *Figures* A.2, A.3 and A.4). While the error is still large, this minute improvement can be used to motivate the need to explore more models and identify one with minimal relative error.

- **Wind Speed**: Even though the wind speeds in *Section* 4.5 are comparable to some degree, it is essential to have a system to choose the point cloud data points as accurately as possible to minimise the gross human error when selecting them manually. The sheer number of data points highlights the difficulty in doing this. Superimposing the wind domain over the data points, and then aligning the coordinate systems of the two models to narrow down the element and the respective data points within the selected element, is a good starting point.

- **Turbulent Mixing Length**: The turbulent mixing length describes how far a particle travels before it changes its property. [12] suggests to have a value that is $\approx 70\%$ of the characteristic length.

Figure 5.6 shows the significant reduction in the relative error when using McAdam's Plate model along with the turbulent mixing length (represented by the purple bar).

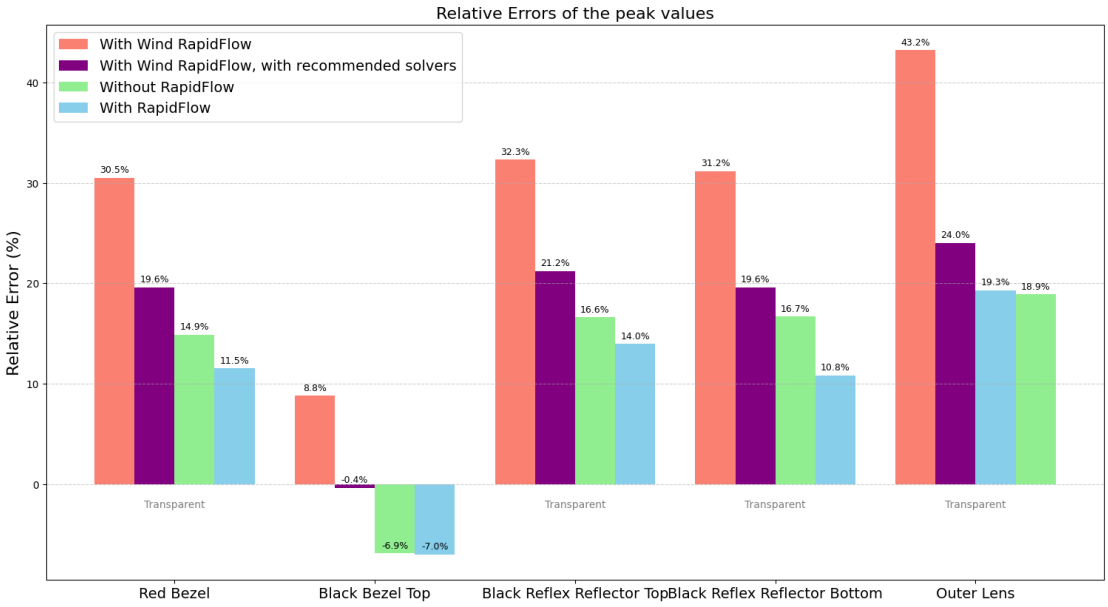

Figure 5.6: Relative error with solvers updated as recommended

Bibliography

[1] E. Fuchs et al. "Strategic materials selection in the automobile body: Economic opportunities for polymer composite design". In: *Composites Science and Technology* 68.9 (2008), pp. 1989–2002. DOI: 10.1016/j.compscitech.2008.01.015.

[2] C. Greenshields. *Notes on Computational Fluid Dynamics: General Principles*. https://doc.cfd.direct/notes/cfd-general-principles/multi-grid-method. CFD Direct. Jan. 2025.

[3] A. Marzo et al. "Comparison of Atacama Desert Solar Spectrum vs. ASTM G173-03 Reference Spectra for Solar Energy Applications". In: *Proceedings of EuroSun 2018*. 2016, pp. 1–13. DOI: 10.18086/eurosun.2016.09.01.

[4] E. Öztürk, M. Aktaş, and T. Şenyüz. "Sun load analysis and testing on automotive front lighting products". In: *Light & Engineering* 01-2020 (2020), pp. 116–122. DOI: 10.33383/2019-026.

[5] T. V. Papathomas. "Celestial illusions and ancient astronomers: Aristarchus and Eratosthenes". In: *Proceedings of SPIE, the International Society for Optical Engineering*. Vol. 5666. 2005, p. 4. DOI: 10.1117/12.602891.

[6] L. Prandtl. "über Flüssigkeitsbewegung bei sehr kleiner Reibung". In: *Verhandl , Intern. Math. Kongr. Heidelberg, Auch: Gesammelte Abhandlungen* 2 (1904), pp. 484–491.

[7] Y. Saad. *Iterative methods for sparse linear systems: Second Edition*. SIAM, 2003.

[8] R. Sachdeva. *Fundamentals of Engineering Heat and Mass Transfer (SI Units)*. 5th. Vols. 1988–2017, pp. 1–626. New Age International (P) Ltd., Publishers, 2017. URL: http://library.um.ac.id/free-contents/index.php/buku/detail/fundamentals-of-engineering-heat-and-mass-transfer-si-units-r-c-sachdeva-30769.html.

[9] T. Shiozawa et al. *Analysis of moisture and natural convection inside an automotive headlamp by using CFD*. Tech. rep. SAE Technical Papers on CD-ROM/SAE Technical Paper Series, 2005. DOI: 10.4271/2005-01-1449.

[10] T. Shiozawa et al. *Analysis of Natural Convection inside an Automotive Headlamp by Using CFD - Temperature Prediction of the Parts by SHT Method*. Tech. rep. SAE Technical Papers on CD-ROM/SAE Technical Paper Series, 2001. DOI: 10.4271/2001-01-0860.

[11] Surface Optics Corporation. *ET-10 HANDHELD THERMAL EMISSOMETER*. https://surfaceoptics.com/wp-content/uploads/2024/11/ET100-Datasheet.pdf. In Surface Optics. 2021.

[12] *Turbulence length scale – CFD-Wiki, the free CFD reference*. https://cfd-online.com/Wiki/Turbulence_length_scale. Accessed: 2025-08-12.

A

Appendix 1

Figure A.1: Segregated rear lamp

A.1 Wind Model Comparison

The McAdams Plate Model was compared with the Universal wind model, with a minute improvement in results.

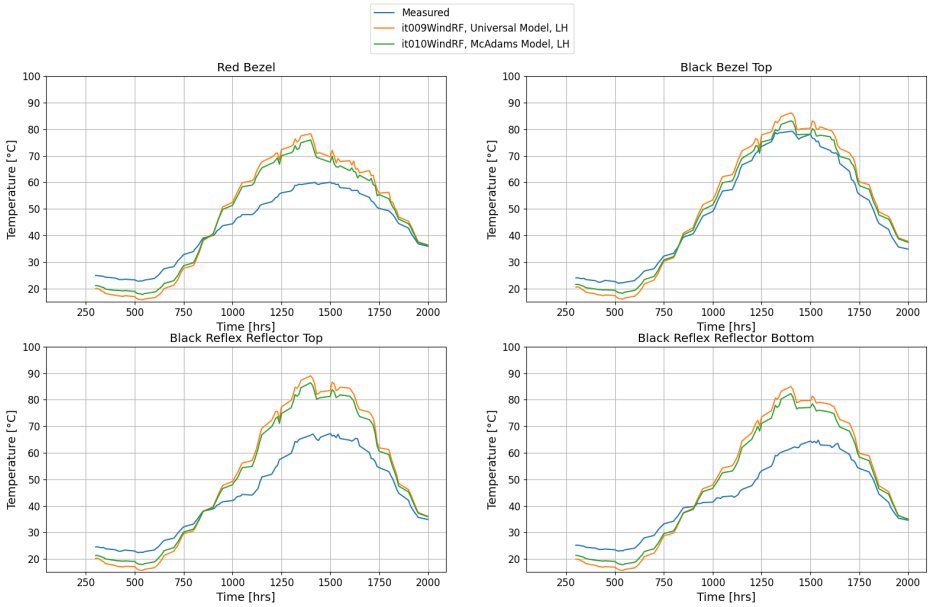

Figure A.2: Wind model comparison, left rear lamp

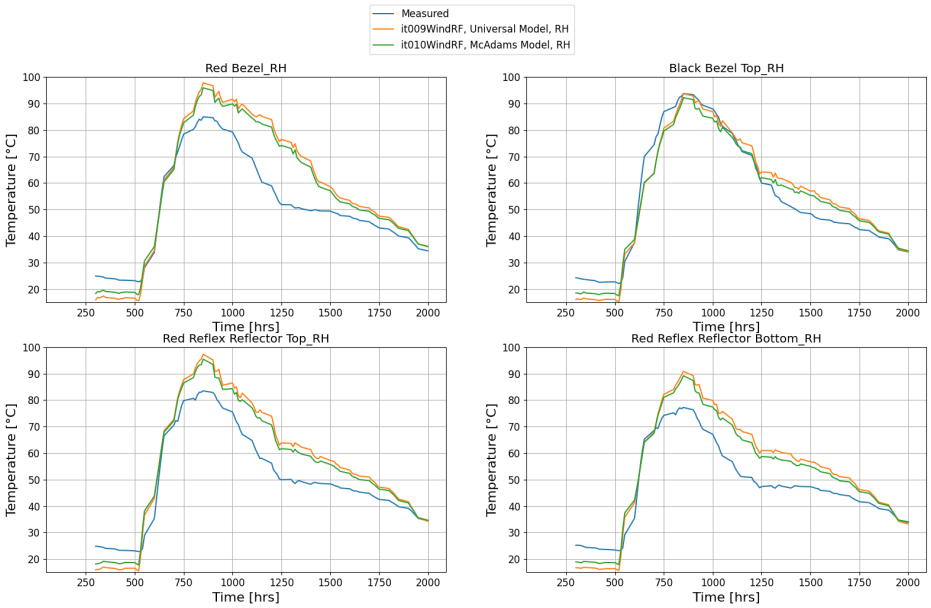

Figure A.3: Wind model comparison, right rear lamp

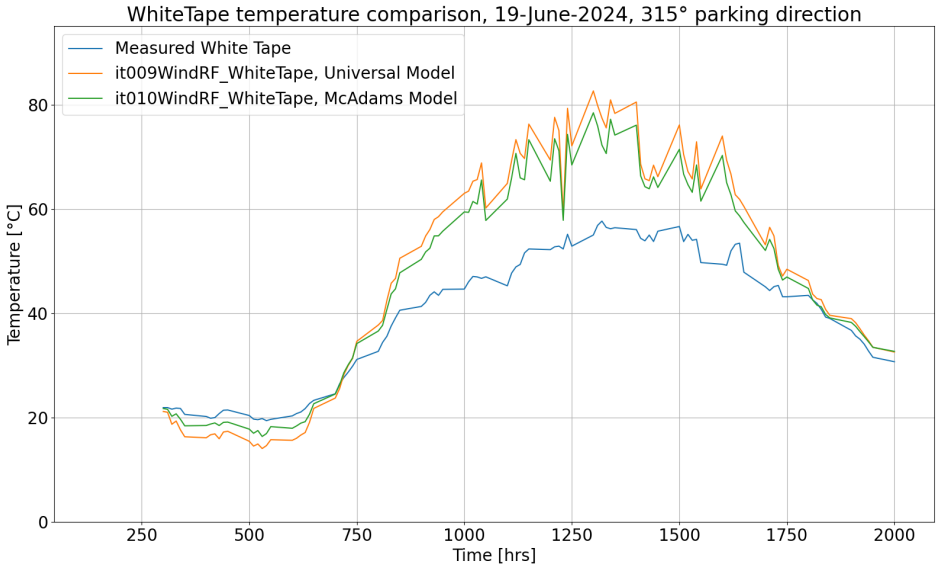

Figure A.4: Wind model comparison, white tape

A.2 Light Source

While this study focused on a parked car scenario, a brief analysis was done with *LEDs* incorporated into the model to understand the effect of a light source in the lamp. It was simulated to be turned on between $10:00-14:00$. Since the data for this scenario was not measured, there was no correlation study done, therefore, these results are primitive and likely require further refinement.

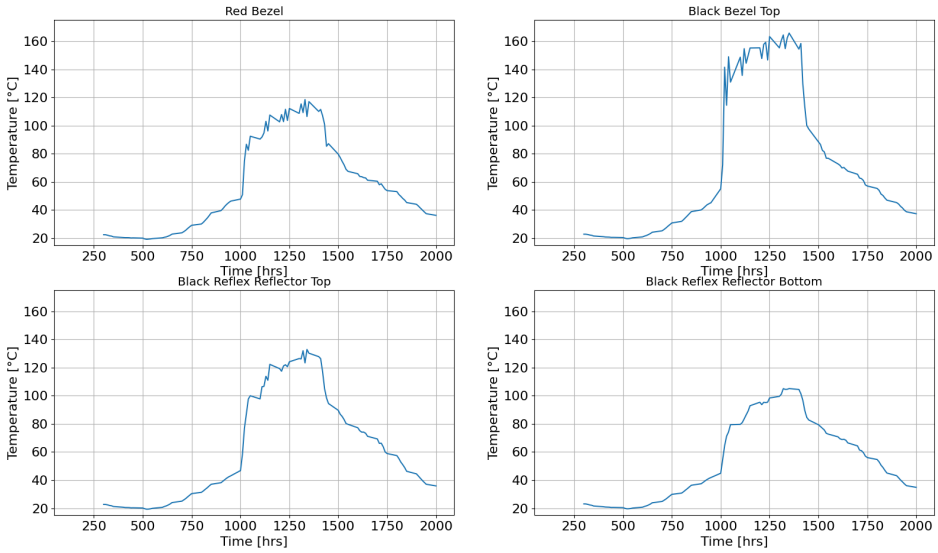

Figure A.5: Left rear lamp, with light source

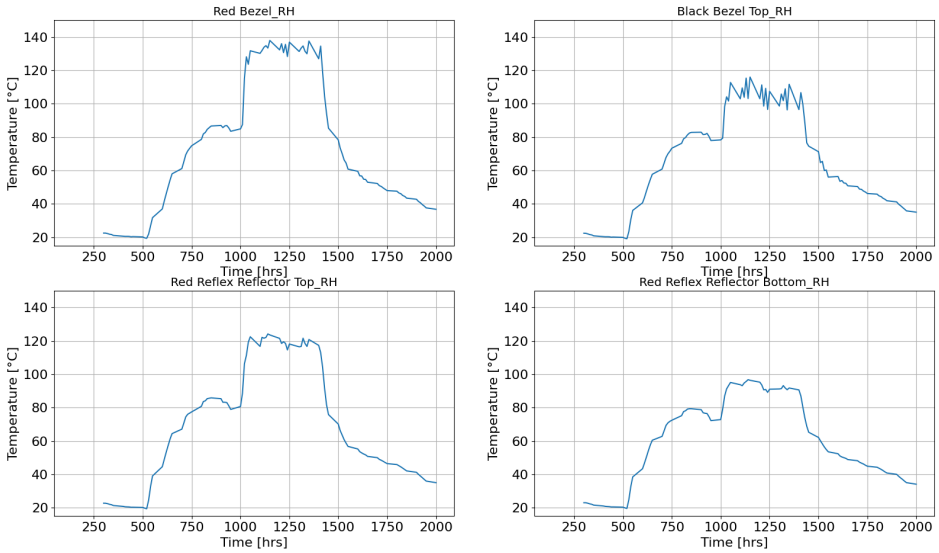

Figure A.6: Right rear lamp, with light source

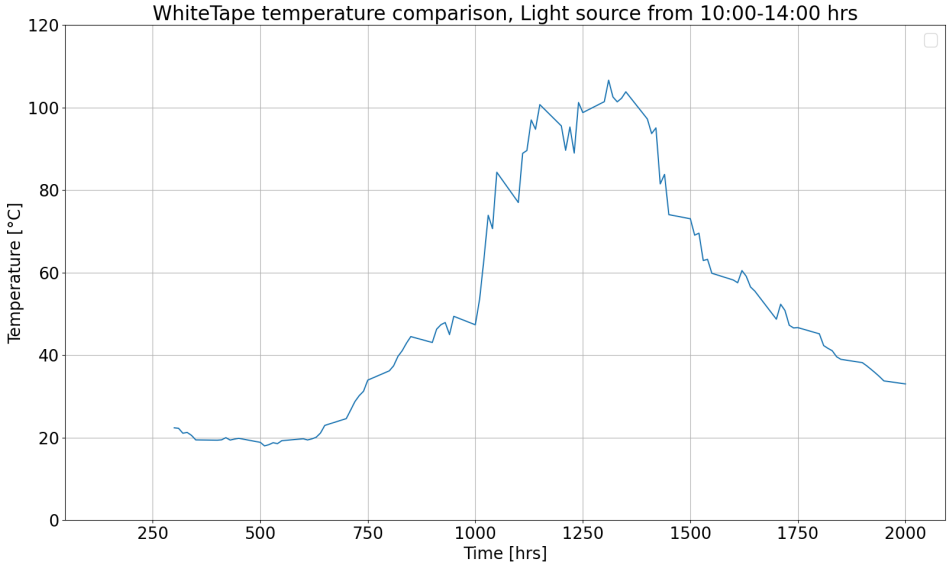

Figure A.7: *Outer Lens* temperature, with light source

A.3 CFL Number Comparison

A comparison of the temperature variation of the *red bezel* thermocouple was made across different CFL numbers.

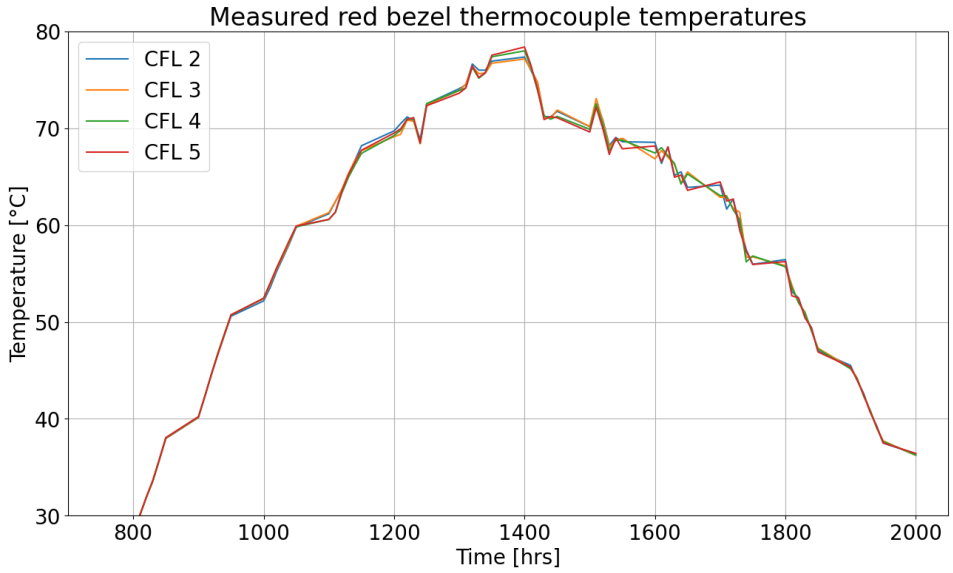

Figure A.8: *Red Bezel* thermocouple temperature variation

Figure A.8 shows that we can decrease the runtime (seen with an increase in CFL number) without a significant change in the results.

DEPARTMENT OF MECHANICS AND MARITIME SCIENCES
CHALMERS UNIVERSITY OF TECHNOLOGY
Gothenburg, Sweden
www.chalmers.se

CHALMERS
UNIVERSITY OF TECHNOLOGY